DIGITALISATION IN MARITIME SAFETY: A BREAKTHROUGH IN HULL STRUCTURAL INTEGRITY ASSESSMENT VIA DISTORTION MODE-BASED CONVERSION ALGORITHMS

Reference NO. IJME 1283, DOI: 10.5750/ijme.v166iA2-A3.1283

D Y Lee, B S Jang,** S W Song, D K Kim,*** Seoul National University, Korea

**These authors contributed equally to this work.
*Corresponding author. D K Kim (Email): do.kim@snu.ac.kr

KEY DATES: Submission date: 02.08.2023; Final acceptance date: 13.12.2024; Published date: 05.06.2025

SUMMARY

With the advent of Industry 4.0, providing enhanced informatics for engineering products is expected to become crucial in establishing their competitiveness. By leveraging the capabilities of digital twins, efforts are being made to enhance the safety margin and operational efficiency of maritime structures, which inherently involve statistical uncertainties due to environmental loads. This study presents a method for constructing a digital twin of hull structures using finite element analysis data, along with a series of validation efforts. The method employs assumptions similar to those used in modal analysis, decomposing the arbitrary deformation states of the hull into a series of eigenmodes. Real-time connectivity between the physical vessel and its virtual twin is established by converting a set of hull strain measurements into eigenvalues. A novel mode selection method is introduced to improve the overall accuracy of structural response estimation. The real-time structural stress traceability of the digital twin model will be further demonstrated through a comparative study on a non-watertight bulkhead model of the vessel. A model validation study will also be presented using actual measurement data from the nearly 13,000 TEU class container ship. Additionally, application examples for the model that can be easily accessed via the commercial marine structure analysis software SESAM have been included to benefit fellow researchers who wish to conduct further studies.

KEYWORDS

Structural integrity, Digital twin, Distortion base mode, Fatigue damage, Spectral fatigue analysis

NOMENCLATURE

[Symbol]	[Definition] [(unit)]
$\underline{\underline{A}}$	Conversion matrix
$\underline{\underline{B}}$	Modal values of estimation target
C_{f1}	Search range coefficient for the first base mode
C_{f2}	Search range coefficient for the second and higher base modes
D_{TMES}	Fatigue damage calculated by rainflow counting the LBSG measured stress time series
D_{TPRD}	Fatigue damage calculated by rainflow counting the estimated stress time series
D_{SMES}	Fatigue damage calculated by spectral fatigue analysis and the LBSG measured stress time series
D_{SPRD}	Fatigue damage calculated by spectral fatigue analysis and the estimated stress time series
D_{SWVX}	Fatigue damage calculated by spectral fatigue analysis and wave radar measured spectrum
E_{ij}	Error between the stress time series measured by i-th LBSG and estimated one for the j-th time shift
F	Structural response of estimation target
$\underline{F^i}$	Structural response of the estimation target for i-th base mode
$\underline{F^R}$	Estimation target response calculated from numerical analysis
$\underline{F^P}$	Estimation target response calculated from conversion model
FM_i	i-th candidate for the first base mode in the RS_1
HBM	Horizontal bending moment [(Nm)]
$\underline{I}$	Imaginary part of numerical analysis result
LBSG	Long base strain gauge
$\underline{\underline{M}}$	Modal values of measured structural response

N_A	Number of all wave load cases of numerical analysis
n_c	Index number for candidate wave load cases
PSD	Power spectral density
$\hat{r}$	Maximum correlation value of the candidate base mode for the selected base modes.
$\underline{R}$	Real part of numerical analysis result
$r(i\|j)$	Correlation between i and j-th base modes
RAO	Response amplitude operator
$\overline{RMSE}$	Averaged root mean square error of conversion model estimate against analysis result
RS_1	Reduced set of wave load cases for the first base mode selection
$\underline{S}$	Scale matrix for normalisation
t_{max}	Maximum time shift in signal synchronising [(sec)]
TM	Torsional moment [(Nm)]
VBM	Vertical bending moment [(Nm)]
$\underline{X}$	Measured structural response
$X_{A,i}$	Time shifted
$X_{M,i}$	Stress signal measured from i-th LBSG
β	Wave heading [(rad)]
Δt	Trial time shift in signal synchronising [(sec)]
$\delta_{i,j}$	Kronecker delta
δt	Time shift increment in the signal synchronising [(sec)]
$\underline{\xi}$	Modal amplitude
ϕ	Wave phase [(rad)]
ω	Wave angular frequency [(rad/s)]

1. INTRODUCTION

The costs and technical difficulties associated with developing data acquisition and analysis systems have decreased to unprecedented levels across all industrial sectors. On the one hand, many stakeholders in the manufacturing industry seem to agree that automating control, inspection, and maintenance will drive innovation. The industrial innovation driven by digitalisation, known as Industry 4.0, is gradually expanding its impact and demonstrating progress in various sectors. Engineering companies that fail to provide better informatics on their products or manufacturing processes may even risk falling behind in competition. In this context, the recent trend in research on digital twins—systems that connect physical entities in the real world with their virtual counterparts—can be understood as a reflection of this phenomenon Liu et al. (2021), Jones et al. (2020).

The applications of digital twins are being explored throughout the product lifecycle, including manufacturing, logistics and service phases. British Petroleum utilises digital twins to monitor and supervise oil and gas production facilities Lattanzi et al. (2021). Applications related to logistics that enhance the supply chain performance of material resources have been observed Abideen et al. (2021). An example of a digital twin operating in the service phase is the battery management system, which has garnered increased attention as a solution to safety performance issues in electric vehicles Shen and Gao (2019). In the service phase, reports of implementations for larger systems, such as buildings El et al. (2022) and bridges Song et al. (2023), are also becoming widespread.

The serviceability of mechanical products includes resistance to fatigue damage and crack growth, ultimate strength, and an adequate range of responses to noise and vibrational excitation. Research is being conducted on digitalisation or digital twin modelling to monitor the serviceability of such mechanical products. To this end, cases utilising Computer Aided Engineering (CAE) or Finite Element Analysis (FEA) data have been observed in the fields of robotics and aerospace engineering Phanden et al. (2021). Additionally, various preliminary attempts related to this can also be found in the field of maritime engineering.

Several frameworks for digital twins have been proposed for use with a variety of structures. Sindi et al. (2024) proposed a Digital Healthcare Engineering (DHE) system consisting of five principal modules to facilitate the lifelong healthcare of ageing ships and offshore structures. Chen et al. (2024) investigated the use of digital twin technology to enhance the reliability of Floating Offshore Wind Turbines (FOWTs), highlighting its role in real-time monitoring, predictive maintenance, and overall operational efficiency. Fujikubo et al. (2024) presented the findings of Japan's research and development project on the Digital Twin for Ship Structures (DTSS), which employs data-driven insights and real-time stress response monitoring. Li et al. (2024a) reviewed the application of digital twin technology in marine structural integrity management, proposing a monitoring framework through model updating, real-time simulation, and data-driven forecasting. Li et al. (2024b) also proposed a digital twin-enabled approach to enhance fatigue reliability and reduce life-cycle costs through data-driven forecasting and reliability-informed inspection.

Efforts to trace the hull's structural response through the digital twin model can be further noted. L'Hostis et al. (2010) demonstrated the Monitas project, which can provide the fatigue lifetime consumption of a hull and support operational decision-making from a full-scale measurement system. Sharma et al. (2018) conducted a study on a reduction-based finite element analysis method to accelerate conventional structural analysis enough to enable real-time finite element analysis. Some researchers have conducted research on the inverse finite element analysis technique to estimate the exact stress field of a local hull structure from measured stress

(Kefal et al., 2015, 2016, 2018; Kobayashi et al., 2019). It was also demonstrated by Matsumoto and Sugimura (2021) that the structural damage on unmeasured locations of a hull could be evaluated from a set of onboard measurements using the Bayesian update and relation-based prediction approach.

On the other hand, some other researchers have estimated the structural response at unmeasured locations using a combination of hull deflection eigenmodes. In this case, by pre-selecting appropriate modes and determining the mode amplitudes by full-scale measurement, it has the significant advantage of being able to recover the different types of structural response at the desired locations and even the deformation of the entire hull structure. Table 1 compares several studies that have used the mode superposition assumption and introduced a series of conversion matrices, have been compared. The conversion matrix, described in more detail in Section 2, is a simple matrix consisting of constant coefficients that transform a given measurement into the structural response of interest (Andoniu, 2019).

The study presented in Table 1 delineates a precise and reliable model focused on estimating crucial design parameters for assessing hull integrity. Interpreting the order of studies summarised in the table as a sequential progression of estimation models with a common purpose may be inappropriate, as they are merely arranged chronologically. Furthermore, this paper primarily explores the use of the conversion model as a tool for constructing digital twins; thus, interpreting these discussions as a further development of those addressed in Table 1 may not be entirely appropriate.

The specific meaning of "Digital Twin" has yet to be clearly defined, and it's likely that readers will have different opinions on its requirements. For convenience, the structural responses typically considered estimable by a structural digital twin are included as estimation targets in Table 1. As discerning readers may already know, not all items listed as estimation targets in the table are essential for evaluating the structural integrity of the hull. It is hoped that the comparison in the table will be seen as a way to assess the level of detail in the descriptions of the models presented in each paper.

Baudin et al. (2013) attempted the classical approach by utilising the natural vibration modes of the hull. As such, Table 1 indicates that mode selection is based on the equation of motion for Multiple Degrees Of Freedom (MDOF) systems. The Response Amplitude Operator (RAO) of the Vertical Bending Moment of a hull girder (VBM) and the long-term values under specific wave spectra were calculated to assess the estimation accuracy of the conversion matrix in the frequency domain.

Koning and Schiere (2014) adopted the operational modal analysis method, where eigenmodes are obtained by transforming signals acquired during operation. The Enhanced Frequency Domain Decomposition (EFDD) method provided by the commercial software Artemis was used for mode selection. Acceleration sensor measurements installed on the actual vessel were converted to estimate hull girder moment and stress, and these estimates were compared to the actual values in both time series and spectral plots. Andoniu et al. (2019) also adopted a similar approach, estimating fatigue damage through rainflow counting.

Table 1. Summary of mode selection approaches and estimation domains in previous research

	Input	Type of Modes	Mode Selection Method	Estimation Target and Domain			
				Hull Girder Moment	Nominal Stress	Hotspot stress	Fatigue Damage
Baudin et al. (2013)	Strain	Natural Vibration mode	MDOF Motion Eq.	Freq.			
Bigot et al. (2013)	Strain	Various Types	Manual Selection	Freq.		Freq.	
Koning and Schiere (2014)	Accelerlation	Operational Modes	EFDD	Time/Freq.	Time/ Freq.		
Bigot et al. (2015)	Hull Girder Loads	Reg. Wave Analysis	Auto Correlation			Time/ Freq.	Spectral
Andoniu et al. (2019)	Strain	Reg. Wave Analysis	EFDD	Time/Freq			Spectral
Song et al. (2024)	Strain	Reg. Wave Analysis	Auto Correlation with PCA			Freq.	
Present Study	Strain	Reg. Wave Analysis	Auto Correlation with Optimisation	Time/Freq	Time/ Freq	Time/ Freq	Rainflow/ Spectral

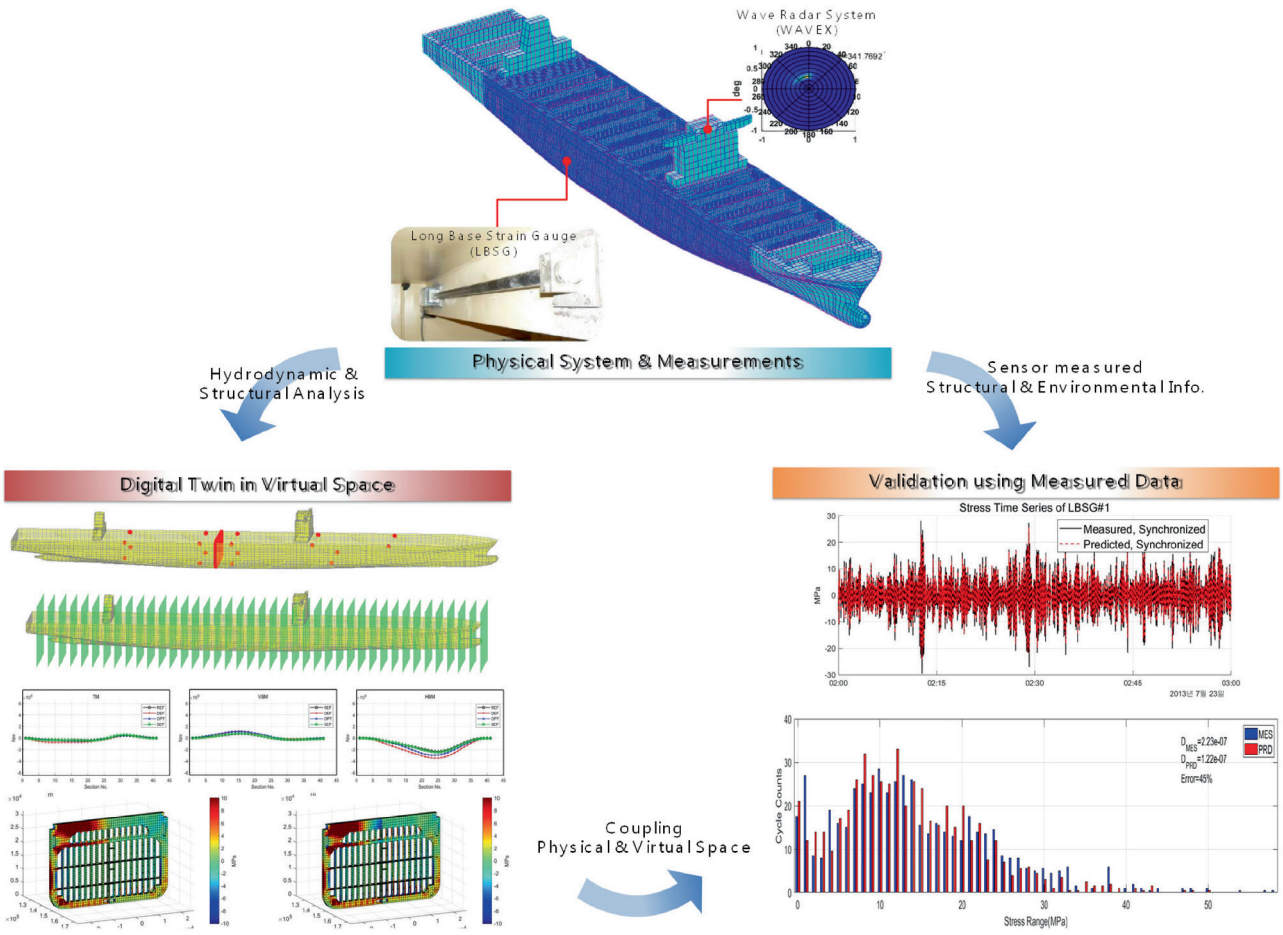

Figure 1. Schematic view of the proposed method and its applicability.

Unlike the case of natural vibration modes, the use of responses to regular waves as eigenmodes necessitates a distinct mode selection method. Adopting the mode superposition assumption implies establishing a mathematical linear vector space to represent any arbitrary hull deformation state. The eigenmodes, which serve as the basis of this vector space, are required to be orthogonal to each other. To assess the orthogonality of these eigenmodes, a method involving the calculation of auto-correlation was proposed by Bigot et al. (2015).

The auto-correlation mode selection method selects the mode that is least correlated with the previously selected modes by inner product. However, this method cannot determine the first mode, which has to be defined by the user. Bigot et al. (2015) used the case of maximum vertical bending as the first mode. Song et al. (2024) proposed the selection of the first mode based on Principal Component Analysis (PCA).

Unlike the traditional natural vibration mode set, where the eigenmode set is derived naturally from the eigenvalue analysis of the MDOF Motion Equation, the autocorrelation-based mode selection method allows for various adaptations in the mode selection approach. For example, questions arise such as how to determine the first mode, how to decide on the total number of modes in the set, or whether there is an optimised mode set for the structural responses being estimated.

This study describes the process of optimising the 1st mode and the total number of modes in the mode selection process. A more detailed description of this mode selection process will be presented in Section 2. Details on how the structural and hydrodynamic analyses were performed will be given in Section 3. After that, the comparison between the mode selection scheme will be given in Section 4 with hull girder moment estimation results.

As in previous studies, the comparison between conversion model estimates and structural analysis results will be given for various hotspots, including hatch coaming corners and stiffener joints, to verify the validity of the established conversion model again. In addition, the stress distribution on the entire bulkhead calculated from the numerical analysis and the one converted from hull stress measurements located in remote transverse sections will be compared in Section 5. This example further demonstrates

that monitoring the hull structural response for multiple structural parts, including transverse structural members, is feasible through the conversion method.

The proposed method is validated with full-scale measurement data from the nearly 13,000 TEU class containership. Cross-validation is performed by comparing the nominal stress estimates on the long base strain gauge (LBSG) location with the real measured ones. The model prediction accuracy in a specific sea condition will be evaluated by converting the calculated stress signals into a response spectrum and comparing it with the third response spectrum obtained by combining the measured wave spectrum from the wave radar and the stress response amplitude operator. The fatigue damage on each strain gauge location is calculated using spectral fatigue analysis and the rainflow counting method. A series of analysis results involving the full-scale measurement data as above will be explained further in Section 6. Overall, the applicability of the distortion mode-based conversion method in building the hull digital twin for structural integrity monitoring is examined.

The schematic view of the innovative method, validation process, and its applicability presented in this study is summarised in Figure 1. The details will be comprehensively covered in Section 2.

2. CONVERSION MATRIX FORMULATION

In the following paragraphs, a linear transformation relationship that converts the measured structural responses into the response of the estimation target is discussed, and the mathematical formulation is as (1).

$$\underline{F} = \underline{\underline{A}} \cdot \underline{X} \tag{1}$$

The $\underline{F}$ in (1) stands for the structural response of the estimation target and the $\underline{X}$ corresponds to the measured structural response (i. e. stress signal measured from LBSGs). $\underline{F}$ can either be the cross-sectional load of a hull girder or the nominal or hotspot stress of local structural parts. This is also true for $\underline{X}$, but only stress signals are used for the scope of this article's discussion. The matrix $\underline{\underline{A}}$ stands for the conversion matrix, which maps the measured stress into the structural response of the monitoring target. As the target load $\underline{F}$ is simply calculated by multiplying the measured stress signals $\underline{X}$ and the conversion matrix $\underline{\underline{A}}$, the location at which the measurement is taken is of great significance. However, this is beyond the scope of the present study and can be addressed in future research.

Taking the mode superposition assumption, the estimated structure response vector $\underline{F}$ can be expressed as the following Equation (2).

$$\underline{F} = \xi_1 \underline{F^1} + \xi_2 \underline{F^2} + \ldots + \xi_{N_m} \underline{F^{N_m}} \tag{2}$$

Here, F^i represents the target structural response vector to be monitored in the i-th base mode and can be determined from numerical analysis. The types of components in the vector $\underline{F}$ are identical to the structural responses being monitored. For example, the vector $\underline{F}$ can be freely composed of hull girder moment, stress, strain, or acceleration, among others. The only limitation is that, being a result of regular wave excitation, the responses must be harmonic. Consequently, structural responses that are not harmonic, such as von Mises stress, cannot be directly constructed within the vector $\underline{F}$. However, since von Mises stress is, in fact, the root mean square of harmonic stress components, it can ultimately be derived from combinations of estimates from various conversion matrices. The matrix that transforms the modal amplitude vector $\underline{\xi}$ into the estimated structure response vector $\underline{F}$ as in Equation (2) above is called Matrix B, and Equation (2) above can be written as Equation (3) below.

$$\underline{F} = \underline{\underline{B}} \cdot \underline{\xi} \tag{3}$$

If the mode superposition assumption is valid, the input structural response vector $\underline{X}$ can also be expressed as Equation (4) as it was in Equation (3).

$$\underline{X} = \xi_1 \underline{X^1} + \xi_2 \underline{X^2} + \ldots + \xi_{N_m} \underline{X^{N_m}} \tag{4}$$

Here, X^i corresponds to the measured structure response vector in the i-th base mode and can also be determined through numerical analysis results. As shown in Equation (4), the matrix that transforms the mode amplitude vector $\underline{\xi}$ into the input structure response vector $\underline{X}$ is called the $\underline{\underline{M}}$ matrix, and Equation (4) can be written as follows.

$$\underline{X} = \underline{\underline{M}} \cdot \underline{\xi} \tag{5}$$

The purpose of the conversion matrix is to obtain an estimated structural response $\underline{F}$ from the measured structural response $\underline{X}$. In Equation (3), the unknown is the mode amplitude vector ξ, and Equation (4) is used to calculate it.

If the pseudo inverse of the $\underline{\underline{M}}$ matrix is applied to both sides of Equation (4), it can be written as follows.

$$\underline{\xi} = \underline{\underline{M}}^{+} \cdot \underline{X}, \qquad \underline{\underline{M}}^{+} = (\underline{\underline{M}}^{T} \underline{\underline{M}})^{-1} \underline{\underline{M}}^{T} \tag{6}$$

If the modal amplitude vector $\underline{\xi}$ in Equation (3) replaced with the one in the right side of Equation (5), it can be written as following Equation (6).

$$\underline{F} = \underline{\underline{B}} \cdot \underline{\underline{M}}^{+} \underline{X} \tag{7}$$

As a result, the conversion matrix $\underline{\underline{A}}$ can be expressed as Equation (7) below.

$$\underline{\underline{A}} = \underline{\underline{B}} \cdot \underline{\underline{M}}^{+} \tag{8}$$

The mathematical formulation is the same as the previous literature (Baudin, 2013; Bigot, 2013, 2015), which initially covered multiple applications of the conversion matrix. In addition, the formulation process and its underlying meaning can also be found in their works.

2.1 DEFAULT BASE MODE SELECTION METHOD

To detail the effects of the optimization of the mode selection method introduced in this paper, the "default mode selection method" will first be described. This method closely reproduces the mode selection approach introduced by the research group of Bigot et al. (2015), although a cross-validation has not been conducted to confirm its exact similarity. Therefore, it would be quite careless to claim that the optimised mode selection algorithm presented in this study represents an improvement over any previously published method. For this reason, this paper aims to create a new control group without optimization to provide a comparison between methodologies, and readers are encouraged to pay attention to these subtle differences.

The following procedure is performed to select the base modes. First, a pool of analysis results is created by performing motion and structural analysis on sine waves of various headings and frequencies. Among them, part of wave load analysis cases showing orthogonal structural behaviour is selected and utilised as base modes. In order to figure out the harmonic responses of hull motion and structure on sine waves, only two cases of analysis are required, the real and imaginary parts. The only difference between the real and imaginary parts is the phase difference by 90 degrees of the ambient sine wave, with all the other conditions, such as frequency and heading, being the same. Analysis results for all the other phases can be regenerated through Equation (9).

$$\underline{F}(\beta, \omega, \phi) = \underline{R}(\beta, \omega)\cos(\phi) + \underline{I}(\beta, \omega)\sin(\phi) \tag{9}$$

Obviously, ω represents the wave frequency, β represents the wave direction, and ϕ represents the phase. $\underline{R}$ and $\underline{I}$ are the real and imaginary parts of the numerical analysis result, respectively. Those can be any among wave amplitude, wave load, ship motion, and structural behavior. However, if the property is not harmonic by its definition, like von-Mises stress, which is always positive, Equation (9) cannot be applied. The set of numerical analysis results which correspond to each load case of a different heading, frequency, and phase as listed in Equation (10) is called 'pool of wave cases. Considering sine wave load cases of N_β wave headings, N_ω frequency, and N_ϕ phases, the pool consists of $N_A = N_\beta \times N_\omega \times N_\phi$ cases of analysis results.

$$\underline{F}(\beta, \omega, \phi) = \{\underline{F}^1 \quad \underline{F}^2 \quad \dots \quad \underline{F}^{N_A}\} \tag{10}$$

Selecting the base modes is identifying a set of $\underline{F}$ orthogonal to each other in the pool of wave cases. The conversion process is similar to linearly regressing the hull deformation state to the vector space, which takes the base modes as the eigenvectors. Therefore, the basis vectors should be orthogonal as possible to each other, and the orthogonality between the bases is evaluated through the following Equation (11).

$$r(i \mid j) = \left(\underline{\underline{S}} \cdot F^i\right) \cdot \left(\underline{\underline{S}} \cdot F^j\right) \tag{11}$$

In the following paragraphs, $r(i|j)$ is called 'correlation', and when the value is small, the case of two wave loads is considered to be orthogonal, otherwise, it is considered to be not orthogonal. Regarding the $\underline{F}^i$ in Equation (11), it is desirable to use the one that can represent the whole ship's structural deformation. The sectional hull girder moment vectors are used in this study. $\underline{\underline{S}}$ is a scaling matrix that normalises $\underline{F}$ to prevent the absolute size of elements constituting $\underline{F}$ from affecting the orthogonality evaluation, and its definition is as shown in Equation (12).

$$\underline{\underline{S}} = S_{ij} = \delta_{ij} \max\left(F_j^i\right) \tag{12}$$

The base mode selection process based on the correlation is presented in Figure 2. The selection method on the left-hand side of the figure corresponds to the one that the optimisation scheme proposed in this paper is not applied, which is also referred to as the default method. The method is similar to the one proposed by Bigot et al. (2015), but some modifications to notations were added to the notations to keep the consistency.

As shown in Equation (11), at least two of the $\underline{F}$ vectors are required to calculate the correlation. However, when choosing the first mode, no $\underline{F}$ has been selected from the pool of wave cases, the dot product in Equation (11) cannot be performed. Therefore, the first mode is arbitrarily selected as the state close to the still water bending case, which is indispensable to express the hull deformed configuration.

In the context of the default mode selection method, the wave load case where the maximum vertical bending occurs is chosen for the first mode. After that, the total number of modes to be selected should be defined. The total number of modes affects the mathematical stability of the pseudo inverse process and should be fairly low than the number of sensor inputs used. It seems desirable to use about half of the total number of sensors as the total number of modes. This is followed by the process of calculating all correlations between the selected mode and all other wave load cases. On the other hand, not all wave load cases in the pool are considered for correlation evaluation with the already selected base modes.

The fact that the correlation coefficient is very low does not necessarily mean that the two considered wave load

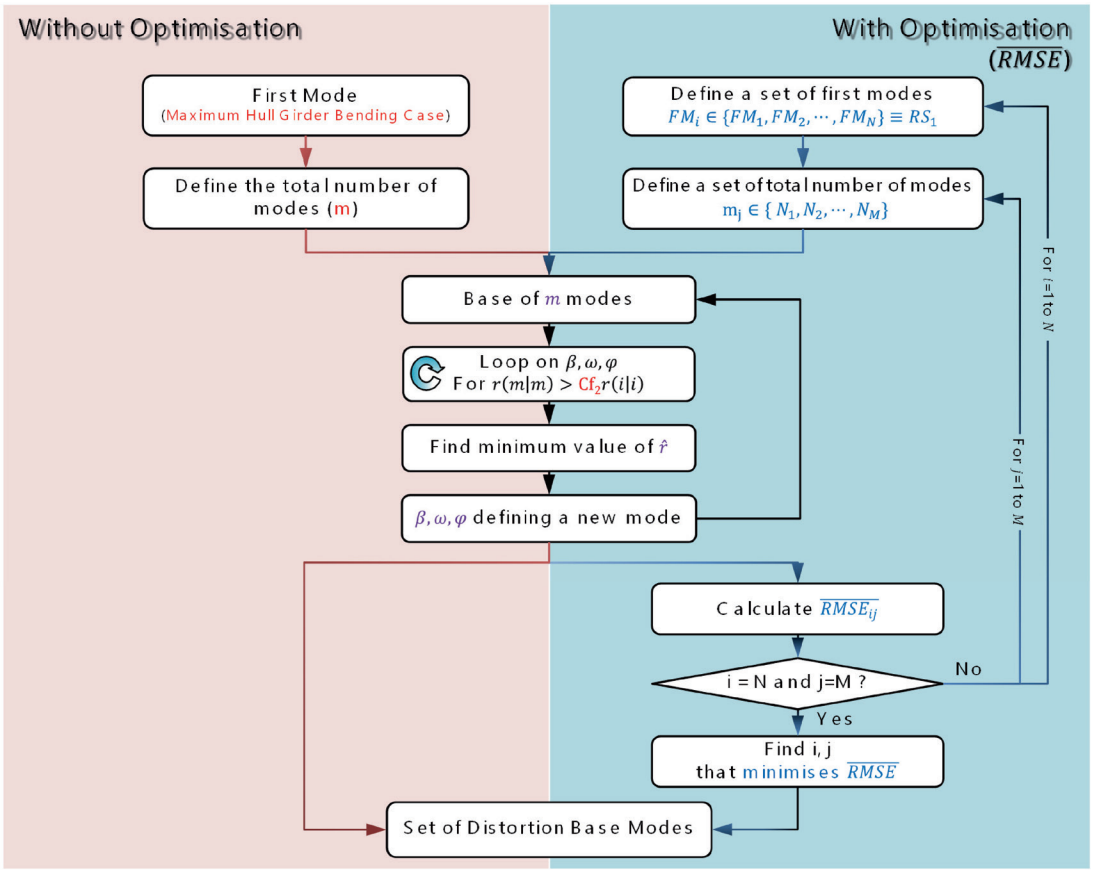

Figure 2. Distortion base mode selection method: without optimisation (Left), with $\overline{RMSE}$ optimisation (right).

cases are orthogonal. There are two main reasons why the correlation value is small. One is that the two vectors are really orthogonal, and the other is that one or both of the two vectors are close to zero. Therefore, to properly establish the base mode set whose components are truly orthogonal to each other, the vectors with norms close to zero should be filtered out before the correlation evaluation. For this, only the wave load cases with autocorrelation over 80% of that of the first mode are allowed to be involved in the correlation evaluation stage.

Here, autocorrelation means the correlation with itself, or in the case of $\underline{F}^i$, it means $r(i|i)$. It is preferable to select a new base mode that is orthogonal to all of the already selected base modes. This can be achieved by evaluating the orthogonality between the new mode and the worst case among all the selected base modes. The maximum value of the correlation coefficient between the previously selected modes and the wave load case evaluated as a new mode is used in this context and defined as $\hat{r}$ as illustrated in Equation (17).

$$\hat{r} = \max_{i \in [1,\, m]} (r(i|n_c)) \tag{13}$$

The lowest $\hat{r}$ means that the wave load case evaluated as a new mode is orthogonal with all the other previously selected modes than other cases in the pool. If the number of already selected modes is defined as m, and the number of wave load cases satisfying the autocorrelation criterion is n_c out of all N_A wave load cases, a total of $n_c \times m$ number of $\hat{r}$ values are calculated for each execution of the innermost mode selection loop. The wave load case that gives the lowest $\hat{r}$ value becomes the new base mode. This process is repeated until the predefined number of base modes are selected.

2.2 OPTIMISED BASE MODE SELECTION METHOD

As mentioned in the introduction, when not using natural vibration modes, various mode selection methods can be explored. Even when limiting the discussion to the correlation-based sequential mode selection method introduced by Bigot et al. (2015), a range of assumptions can be tested. The variation in estimation accuracy of the conversion method based on mode composition is not being explained for the first time in this paper; its potential variability has been mentioned in previous studies. Differences in the accuracy of the conversion method according to the number of modes have been presented by Bigot et al. (2015). Consideration of the accuracy of the conversion method based on mode composition is also mentioned in the study by Andoniu et al. (2019). However,

these studies did not provide tools for quantitatively analysing the accuracy differences in the conversion method based on mode composition.

In this study, the root mean square error (RMSE), a parameter that quantifies the accuracy of the conversion model estimation based on mode composition, is defined. $\overline{RMSE}$ is a widely used parameter across various fields, and in this study, it similarly represents the average error between the conversion method estimate and the actual values obtained from numerical analysis. Its definition is presented in Equation (14).

$$\overline{RMSE} = \frac{1}{N_A}\sqrt{\sum_{i}^{N_A}\left(\underline{F_i^R} - \underline{F_i^P}\right)^2} \tag{14}$$

N_A in Equation (14) means the number of all wave load cases. The estimation target of the conversion model or the vectors used to evaluate the mode orthogonality is used as the vector $\underline{F}$ in Equation (14). $\underline{F}$ has a superscript, and the letter R from the word 'reference' means that the vector is imported directly from numerical analysis. The superscript P implies prediction and means the value estimated from the conversion matrix. That is, $\overline{RMSE}$ means the standard error of the conversion model estimation with respect to the vector obtained directly from numerical analysis. Therefore, a smaller $\overline{RMSE}$ value indicates that, on average, the accuracy of the conversion method is high across all numerically considered cases. The composition of the conversion matrix is entirely dependent on the selected eigenmodes, allowing for the evaluation of how accurately the mode configuration predicts a given structural response.

Adopting the mode superposition assumption means approximating the arbitrary deformation state of a structure using a linear vector space composed of eigenmodes. The basis of this linear vector space is required to be orthogonal, and the correlation mentioned in Section 2.1 can be interpreted as a means of assessing this orthogonality. Additionally, the basis vectors must not be the zero vector, and the requirement for autocorrelation to exceed a certain threshold can also be understood in this context. The mode selection algorithm can be viewed as the process of identifying a set of basis vectors that can effectively approximate pool of all other vectors from regular wave analysis.

To describe the behavior of the correlation-based mode selection algorithm introduced in this paper within this vector space, the process can be outlined as follows. First, an arbitrary vector with a sufficiently large norm is selected, ensuring it is not the zero vector. Since this vector is not the zero vector, a correlation value close to zero indicates orthogonality, thus ensuring it is non-trivial. Next, a second basis vector is selected that is the most orthogonal to the first one while having sufficiently high autocorrelation, ensuring it is also not the zero vector. Following this, the next vector that is most orthogonal to the already selected vector set can be identified. Through this series of steps, a predetermined number of basis vectors can be selected.

This series of mode selection methods can be defined as a type of function that takes the first mode and the total number of modes as inputs and returns the set of eigenmodes as output. The composition of the eigenmode set has been shown to depend on these two input parameters within the range we have observed. The performance and accuracy of this function can be evaluated using the previously introduced $\overline{RMSE}$. Naturally, the $\overline{RMSE}$ values are limited to the range defined by N_A and the total number of modes attempted. Within this constrained range, it is always possible to find a minimum $\overline{RMSE}$ value. The optimization process proposed in this paper refers to the procedure of identifying this minimum value.

3. NUMERICAL INVESTIGATION

The series of processes described in Section 2 assumes that hydrodynamic analysis in the frequency domain is conducted using a panel code that solves for diffraction and radiation potential flow. A key finding from this study is that the loading conditions of the hydrodynamic and structural analysis model used to construct the conversion model must be the same as those of the physical twin or its numerical equivalent. In the context of an oil tanker, the loading condition refers to the tank filling ratio, while for a container ship, it includes both the tank filling ratio and the arrangement and mass of the container cargo. It has been confirmed that applying a conversion model with differing loading conditions results in overall lower accuracy. Since the content to be introduced after Section 4 includes an evaluation of the estimation accuracy of the conversion model using data measured from actual ships, it is crucial to accurately reflect the loading conditions of the physical ship in the numerical calculations. This topic will be addressed in this section.

A set of full-scale measurement data from a real containership was utilised, and numerical analysis on its finite element model was conducted to validate the established conversion model. The vessel used in the study is a nearly 13,000 TEU class container ship. Long Base Strain gauge (LBSG), accelerometer, Inertia Motion Unit (IMU), and Wave radar system (WAVEX) were installed on the ship to provide data related to the ship's structural response. The WAVEX provided information on the surrounding sea conditions, such as sea wave spectrum, significant wave height, and wave peak period. Of the large volume of data measured for about two years from 2011 to 2013, only the ones measured in specific periods by expecting a sufficiently large structural response and good data quality were used for validation. Based on the information obtained from the WAVEX system, time zones with a sufficiently large significant wave height were selected. As a result, a total of three time zones were specified between June and July 2013.

In the case of time zone 1, it was early dawn on July 23, 2013, close to the head sea condition. Time zone 2 is the same day as time zone 1, but it is seen that the significant wave height is larger than the case of time zone 1. In addition, time zone 2, the mean wave heading is closer to the oblique sea than in the case of time zone 1. In the case of time zone 3, it is the harsh wave condition whose wave height reaches 5 meters. Judging from the wave spectrum, it is seen that the wave heading is close to the beam sea condition. The final verification process of the model is performed through full-scale measurement data, in particular, the measured stress signals. The contents of this study will be further introduced later in Section 5.

For the conversion model estimates and measurement data to match, the numerical analysis conditions of the vessel must be similar to the measurement environment. One of the requirements to be satisfied to perform numerical analysis close to reality is the loading condition. On the other hand, detailed information on the loading condition, such as container placement and tank filling ratio, could not be obtained. Instead, if the draft of the analysis environment and the actual environment are the same, the overall load condition is assumed to be similar to the actual environment.

However, the onboard measurement system could not acquire detailed information on the draft in those time zones. Therefore, the data compilation of the full-scale measurement campaign conducted by Bureau Veritas on 13,000 TEU container ship was referred to. After examining the draft data, it was confirmed that the 23rd design loading condition has a draft of 14.26m, which is most similar to the draft at time zones 1 and 2. Therefore, whole ship numerical analysis was performed for loading condition 23 (LC23).

Figure 3 shows the container placement for LC23 and the panel model for motion analysis. Using the generated numerical model, motion- and structural-analyis were performed by the seakeeping simulation code (ISTAS) developed by Korean Register (KR). Unfortunately, due to the proprietary nature of this internally developed software, official launch version information cannot be disclosed. The draft of the ship was set to 14.26m as indicated in LC23, and the forward speed was assumed to be 7.7m/s. A series of numerical analyses were performed for a total of 12 directions from 0 degrees to 330 degrees with 30-degree intervals. For each direction, a total of 22 wave frequencies ranging from 0.05 rad/s to 1.1 rad/s were considered. The wave pressure load calculated through motion analysis was applied to the finite element model of the whole ship structure to calculate the structural response. Since numerical analysis is performed for two different sine wave phases, real and imaginary parts, 528 analysis results in response amplitude operator (RAO) form were calculated.

The conversion model studied in this paper is based on the mode superposition assumption. This theoretically

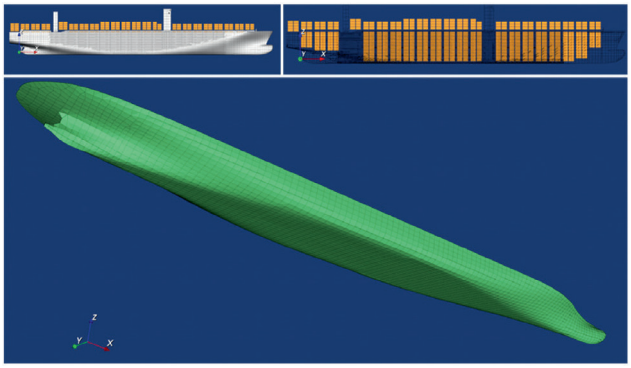

Figure 3. Analysis model for design loading condition 23: container placement (Top), panel model (Bottom).

enables the method to estimate any type of structural response in any location in the hull structure. Therefore, to fully describe the applicability of the conversion model to the hull digital twin, it would be ideal to present the entire structural response conversion result (i. e. hull deformation shape) for the whole ship hull finite element model. On the other hand, for this, not only a massive amount of matrix computation but also an advanced level of rendering technique is required, which is quite hard to perform. The hull can be regarded as a beam structure, and the longitudinal stress applied to the structure can be determined if the moment applied to the cross-section of the hull is known.

Therefore, validation of the conversion model for longitudinal structural members is performed indirectly by checking the agreement between the actual and estimated hull girder moment distribution. The hull girder moment is evaluated for the cross-sections indicated by the green rectangles in Figure 4 above. The hull girder moment is calculated by integrating the surface wave pressure from the motion analysis model. The still water bending moment component is not considered, and only the dynamic component due to wave pressure is considered. For each cross-section, three directional moment components are considered. The moment components parallel to the global x, y, and z axes are sequentially expressed as Torsional Moment (TM), Vertical Bending Moment (VBM), and Horizontal Bending Moment (HBM). The accuracy of the conversion model estimate for the transverse structural member is confirmed by comparing the stress distribution of the non-watertight bulkhead shown in the red squared part at the top of Figure 4.

The conversion model has been validated for the major hotspot locations where it is expected to be vulnerable to fatigue damage. As shown in Figure 5, the estimation accuracy of the conversion model is examined for three hotspots in the hull structure. The fine-meshed model of each part is illustrated in Figure 5. The first hotspot is at the stiffener joint on Frame 78 near the midship. It can be seen

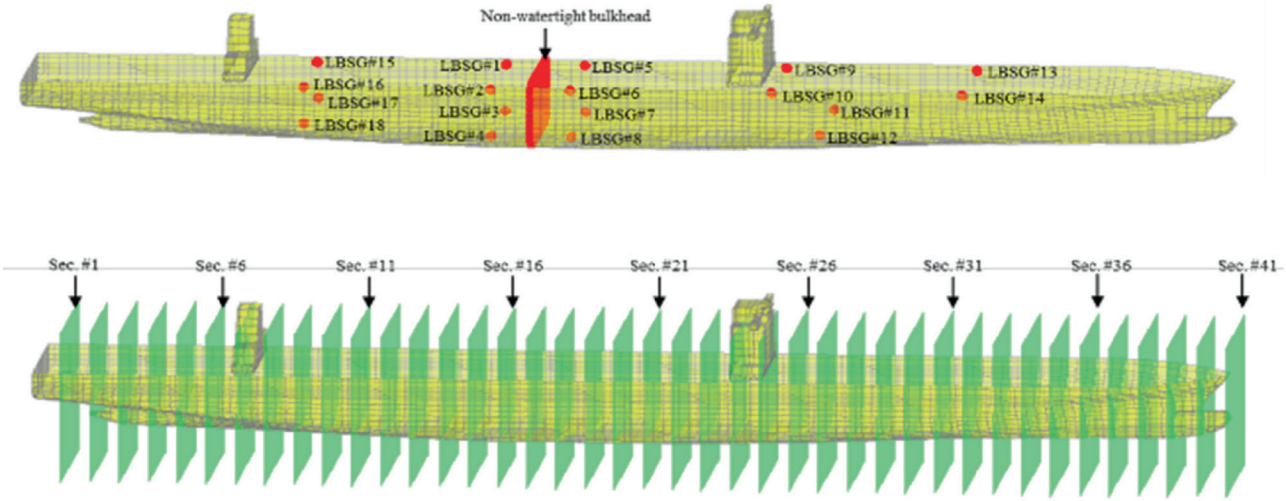

Figure 4. Finite element model with result extraction position marked: Long base strain gauge (LBSG) and non-watertight bulkhead (Top), load cross-section for hull girder moment calculation (Bottom).

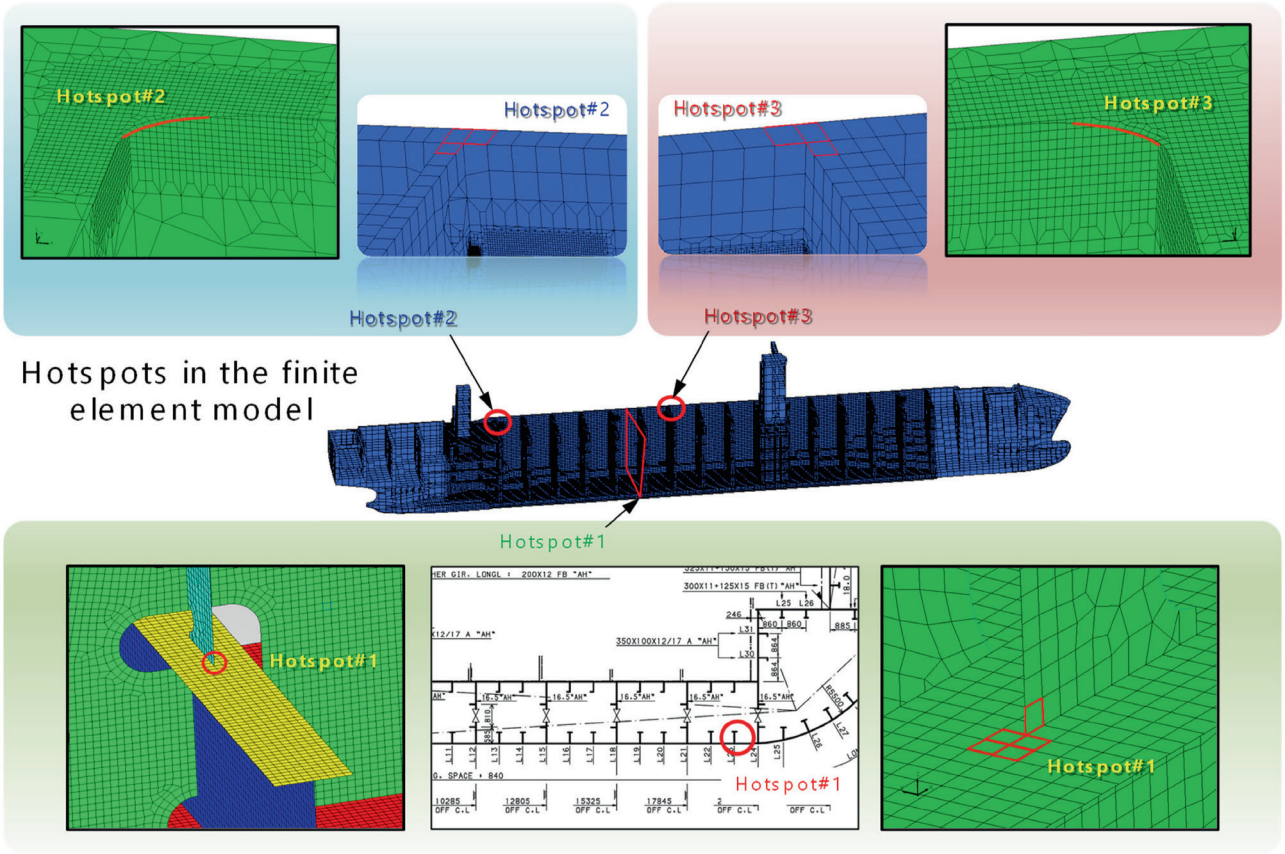

Figure 5. Hotspot in the finite element model including hotspot position in the whole ship model and enlarged view of the hotspot.

Table 2. Selected base mode information for 'DEF', 'OPT' and 'SEP' cases.

	DEF Case Base Modes			OPT Case Base Modes			SEP Case TM Base Modes			SEP Case VBM Base Modes			SEP Case HBM Base Modes		
Mode No.	ω (rad/s)	β (deg)	ϕ (deg)	ω (rad/s)	β (deg)	ϕ (deg)	ω (rad/s)	β (deg)	ϕ (deg)	ω (rad/s)	β (deg)	ϕ (deg)	ω (rad/s)	β (deg)	ϕ (deg)
1	0.45	180	236.57	0.45	180	61.71	1.10	270	92.57	0.75	60	288.00	0.45	240	113.14
2	0.60	240	339.43	0.95	90	61.71	0.60	330	195.43	0.45	180	123.43	0.65	60	298.29
3	0.30	90	288.00	0.30	270	288.00	0.55	60	102.86	0.50	180	133.71	0.70	60	216.00
4	0.70	300	164.57	0.60	60	144.00	0.55	30	102.86	0.50	120	164.57	0.80	120	205.71
5	0.70	60	164.57	0.60	300	144.00	0.60	120	102.86	0.35	180	164.57	1.05	60	236.57
6	0.60	60	144.00	0.65	120	277.71	0.80	30	298.29	0.75	60	30.86	0.50	60	339.43
7	0.75	300	102.86	0.70	300	349.71	0.70	30	216.00	0.50	120	277.71	0.85	120	82.29
8	1.00	270	298.29	0.70	60	349.71	0.60	150	61.71	0.40	30	72.00	1.10	60	329.14
9	0.65	240	51.43	0.65	240	277.71	0.65	30	318.86	0.40	0	10.29	0.55	120	164.57
10	–	–								0.40	150	257.14	1.10	60	329.14
11	–	–								0.50	180	72.00			
12	–	–								0.55	120	51.43			
13	–	–								0.60	120	113.14			

that multiple finite elements are located for each hotspot location. For each load case, the largest response among them was taken as the representative stress RAO of the part.

The second and third ones are at hatch coaming corners of the container ship. The second hotspot is located right in front of the engine room. The third one is located at frame number 85 near the midship. Figure 5 shows a coarse mesh where hatch coaming corners are not modelled in detail. As with the first hotspot, the most significant principal stress among the elements indicated by the red line was taken as the representative stress RAO for the part. The accuracy of the conversion model for various structural members will be examined through the case studies mentioned above.

4. MODEL VALIDATION

In the validation process, three different mode selection schemes are performed. In the following paragraphs, these mode selection processes are denoted as 'DEF', 'OPT' and 'SEP', respectively. The 'DEF' case is a default mode selection process as described in Section 2.1. The 'OPT' case proposed in this study is a mode selection process using the optimization process with the girder moment as the objective function. Lastly, the 'SEP' case is an eigenmode selection process optimised for each of the three directional components of the hull girder moments, i.e., TM, VBM, and HBM.

The base modes selected by two different methods, 'DEF' and 'OPT', are shown in Table 2 below. The coefficients for the optimisation range were set to be $[C_{f1}, C_{f2}] = [0.8,0.8]$, and the total number of modes was tried from seven to 13 by an interval of 2 modes. As a result, a total of 9 base modes were selected in the 'OPT' case. The total number of modes for 'DEF' case were determined to be the same as the 'OPT' case. This is because if the total number of modes is different, it is challenging to determine which condition affected the model accuracy. The base modes selected by the 'SEP' method are also shown in Table 2. For the 'SEP' case, the coefficients for the optimisation range were set to be $[C_{f1}, C_{f2}] = [0.5,0.3]$ for TM and HBM. For VBM, $[C_{f1}, C_{f2}] = [0.3,0.8]$ was used, and the trial range for the number of modes is the same as the 'OPT' case. The total number of modes was determined to be different for each type of hull girder moment, nine modes for TM, 13 modes for VBM, and 11 modes for HBM.

5. VALIDATION BY NUMERICAL SIMULATION DATA

Before applying the full-scale measurement data, the conversion model is validated by comparing its estimates with the numerical analysis results. Sensor measurements are required to compute the model estimates. In the case of actual ship application, the sensor measurement corresponds to the hull stress measurement of the strain gauges. However, for the validation process illustrated in this section, the stress signals calculated from structural analysis results replace the measured stress signals. In other words, it was assumed that the stress was accurately obtained from the strain measured in real time. If the estimates obtained from these numerically calculated

inputs match the analysis results, the established conversion model can be assumed to be valid, and this process is illustrated in Figure 6.

All the hull structural responses in this validation process are generated by RAO. Both the structural response and surrounding sea waves are calculated in the 'wave and response generation' part on the left of Figure 6. The stress response produced by the stress RAO and 'wave and response generation' part becomes the conversion model input vector X below Figure 6. The base mode selection and the conversion matrix building process are located in the upper middle of Figure 6.

For the base mode selection process, three different selection schemes are tried, the default method, optimisation method, and separate optimisation method. All of them require the hull girder moment RAO for the orthogonality evaluation. As a result of the base mode selection process, a set of distortion base modes is determined. The modes are specified by the wave heading, frequency, and phase, which are the applied wave load condition of the hull structural analysis. The conversion matrix is then composed based on the estimation target RAO, sensor RAO and base mode information with the conversion model estimate is created from the estimation target RAO and 'Wave and Response generation' part. The combination of input vector 'X' and the conversion matrix produces the model estimates. Since different conversion matrices are created according to different types of mode selection schemes, different types of estimates are also generated. The comparison between the estimates of each class and the reference will be made for the hull girder moment on load cross sections, hotspot stress, and stress distribution of the non-watertight bulkhead.

Figure 7 shows the estimation result of each hull girder moment component for an irregular sea wave of $\bar{\beta} = 120^{\circ}$. To create the irregular sea wave environment, cosine 2^{nd} spreading and significant wave height of 5m, the peak period of 10 second JONSWAP wave spectrum was used in the wave and response generation part. A total of three different base mode selection schemes were used to generate hull girder moment estimates. The plots in the second row of Figure 7 show each type of estimate and the actual hull girder moment distribution (REF). In the case of TM and VBM, the reference and estimated results of all cases show good agreement. On the other hand, in the case of HBM, estimates from the default method show more inaccurate results than the ones from optimised methods. However, the difference in accuracy between the results of OPT and SEP cases, for which the optimisation is applied, is not clearly observed.

The graphs on the left of Figure 8 show the time series of hull girder moment changes for a specific cross-section for each case. Only the results for the specific load cross-sections where the maximum hull girder moment is expected are attached, and the referred sections are different for each moment component. The graphs arranged in a total of three rows include results for oblique sea wave conditions. The plots in the first row show the change in TM at the 10th load cross-section. The plots in the second and the third row illustrate the time changes of VBM and HBM values at the 20th load cross-section, respectively. The solid black line in each graph (Figure 8) represents the actual value obtained from numerical analysis.

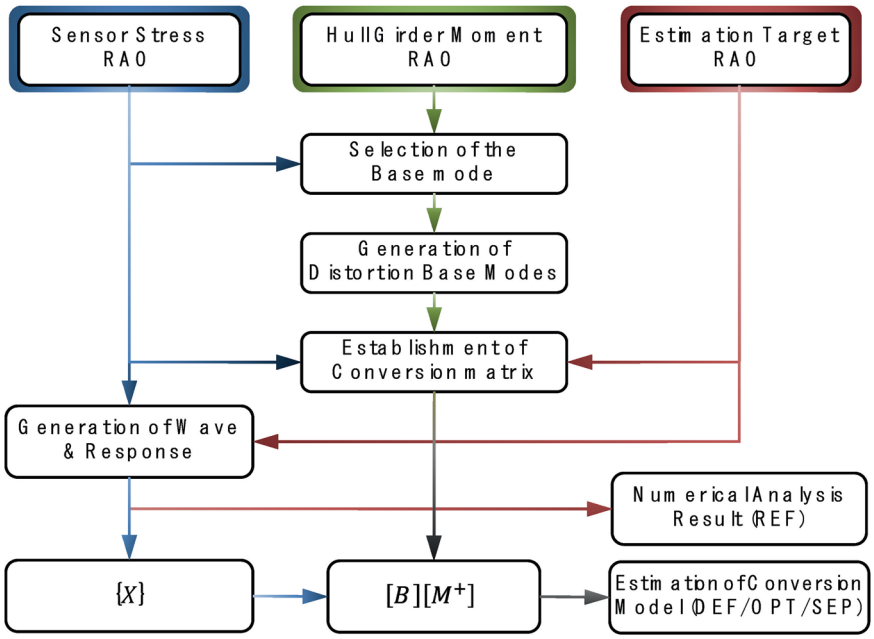

Figure 6. Validation process using numerical analysis results.

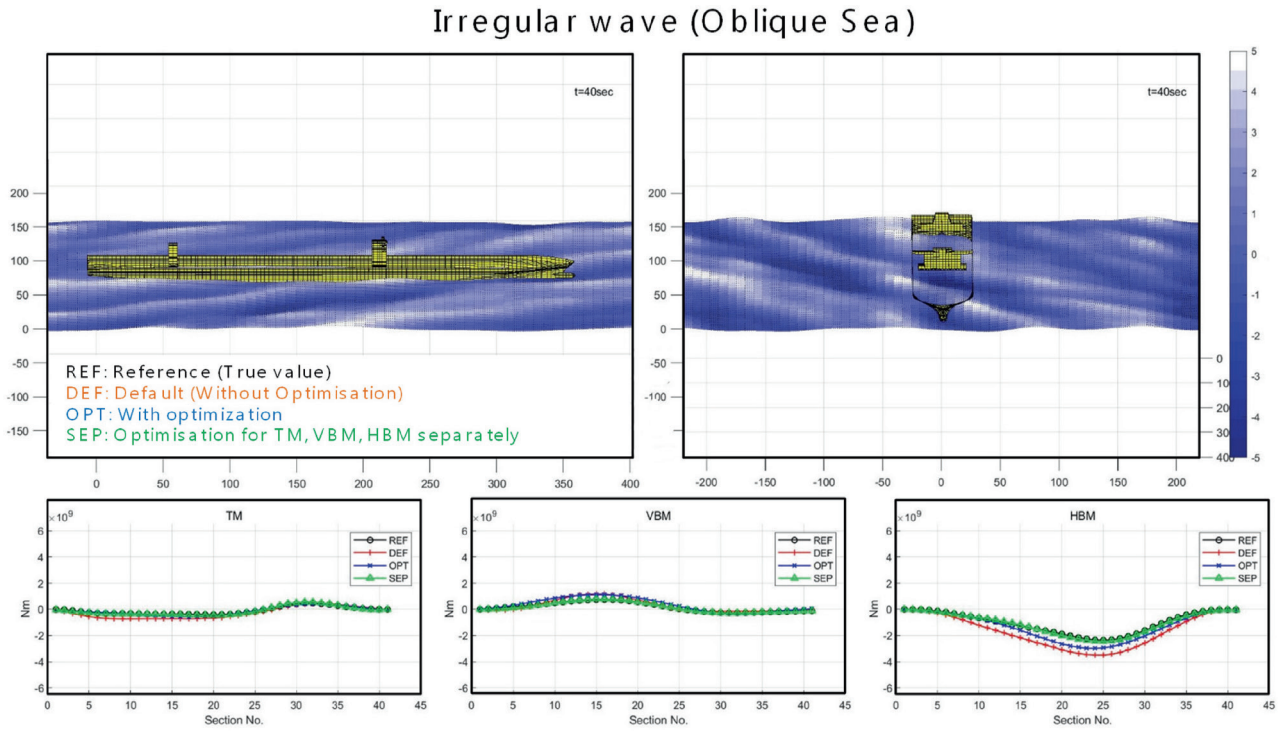

Figure 7. Comparison of hull girder moment distribution in irregular oblique sea wave.

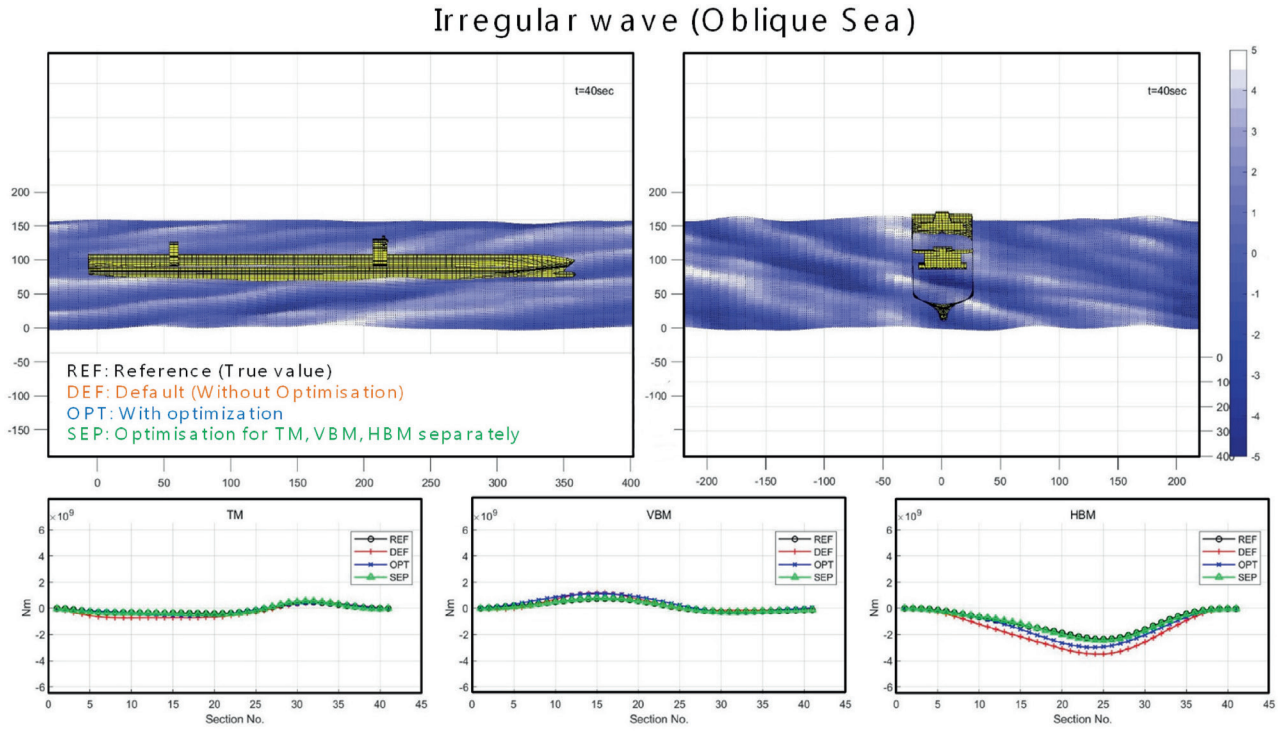

Figure 8. Hull girder moment changes in time series at load cross sections for TM (upper left), VBM (middle left), HBM (bottom left), Stress time series at hotspot 1 (upper right), 2 (middle right), 3 (bottom right).

The coloured lines are the results estimated from the conversion model. The legend for each item can be found in the upper left of the figure. Except for the VBM result shown in the second row of the figure, all the red lines are detached from the black one, the reference. This shows that the conversion matrices from the optimised selection methods result in more accurate hull girder moment estimates, as in the results shown in Figure 8.

Figure 8 also shows the hot spot stress estimation results for the oblique sea waves. The black-coloured lines labelled as 'REF' is the true value of the maximum principal stress on hotspots directly imported from the structural analysis result. The 'OPT' case conversion matrix estimates are drawn in the solid blue line. The distortion base modes included in the 'SEP' case were selected to minimise the estimation error of each directional component of the hull girder moment.

Therefore, the 'SEP' case base mode set and corresponding conversion model are inappropriate for estimating the stress at hotspot locations, and it was excluded from the hotspot stress comparison in Figure 8. The blue line estimated from the optimised method is closer to the reference value for all hotspot positions than the red line estimated from the default method.

The error between the numerical analysis results and the conversion estimates of the hull girder moment RAO can be calculated for regular wave load cases. By summing these errors to obtain an average across all the regular wave load cases, the $\overline{RMSE}$ values were calculated as 39.99 MN for the 'DEF' case, 19.2 MNm/m for the 'OPT' case, and 17.21 MNm/m for the 'SEP' case. This indicates that the use of the optimised mode selection algorithm leads to an overall improvement in the accuracy of the conversion method.

The objective function of optimisation, $\overline{RMSE}$ is defined to represent the standard hull girder moment estimation error. Thus, the optimisation process is expected to increase the accuracy of conversion model estimates on the hull girder moment. Though the base mode selected through the optimised method is used, the estimation accuracy of various structural responses, such as hull girder moment and hotspot stress, is improved overall. This seems to be because the base mode-set selected through the optimised method better represents the overall deformation state of the hull structure.

The bulkhead stress estimation results in irregular ocean waves are illustrated in Figure 9. The stress contour on the bulkhead expresses the membrane stress in the local coordinate x-direction of each element. Since the comparison between the default and optimised methods seems to be sufficiently given, the default case results are not presented in this example. On the left column in Figure 9, the stress contours calculated directly from the numerical analysis result are displayed, and on the right, the stress contour estimated from the conversion model is shown. The stress contours are presented in three rows, which differ in the time step when the contours are captured. The first row of the figure shows the result at ten seconds in the simulation time, while the second and third rows display the results at twenty and thirty seconds.

In both the reference stress distribution and the estimated one, a stress concentration region of similar shape and strength is observed at the upper left of the bulkhead. In the first and second rows in Figure 9, the stress concentration area coloured in red shows a similar distribution in both reference and estimated results. However, the estimated contour at the third row seems different from the reference contour. The error is thought to become more obvious when the hull deformation is small since this results in a small input for the conversion model, making it challenging to identify how the vessel is being deformed clearly. However, the difference in stress contour may not significantly affect the fatigue damage estimates.

6. VALIDATION BY FULL-SCALE MEASUREMENT DATA

The validity of the established conversion model was examined through comparative studies, but it is still uncertain whether it would achieve acceptable accuracy in onboard applications. If the match between the estimated and measured structural response is confirmed, it becomes more evident that the model estimates represent the actual hull structural behaviour. The validation process using the full-scale measurement data is illustrated in Figure 10. The ensuing series of plots presented in this section may initially prove challenging to interpret. In order to facilitate understanding of their composition and implications, Figure 10 includes some visual aids displaying the figure numbers alongside the corresponding data types.

The measured time series stress obtained from the LBSGs and wave spectrum measured by wave radar installed on the 13,00TEU class container ship are utilised in the process. The Stress RAO from structural analysis and Hull girder load or hull girder bending moment RAO from hydrodynamic analysis are also utilised for base mode selection and conversion matrix assembly.

The measured stress may be used as the conversion model input, but no data measured for the sole purpose of estimated stress validation does exist. On the other hand, the stress on an LBSG position can be predicted using the time-series stress measured from the other LBSGs, and this can be compared with the time-series stress measured directly at that location. Cross-validation of the conversion method is performed by checking the match between the

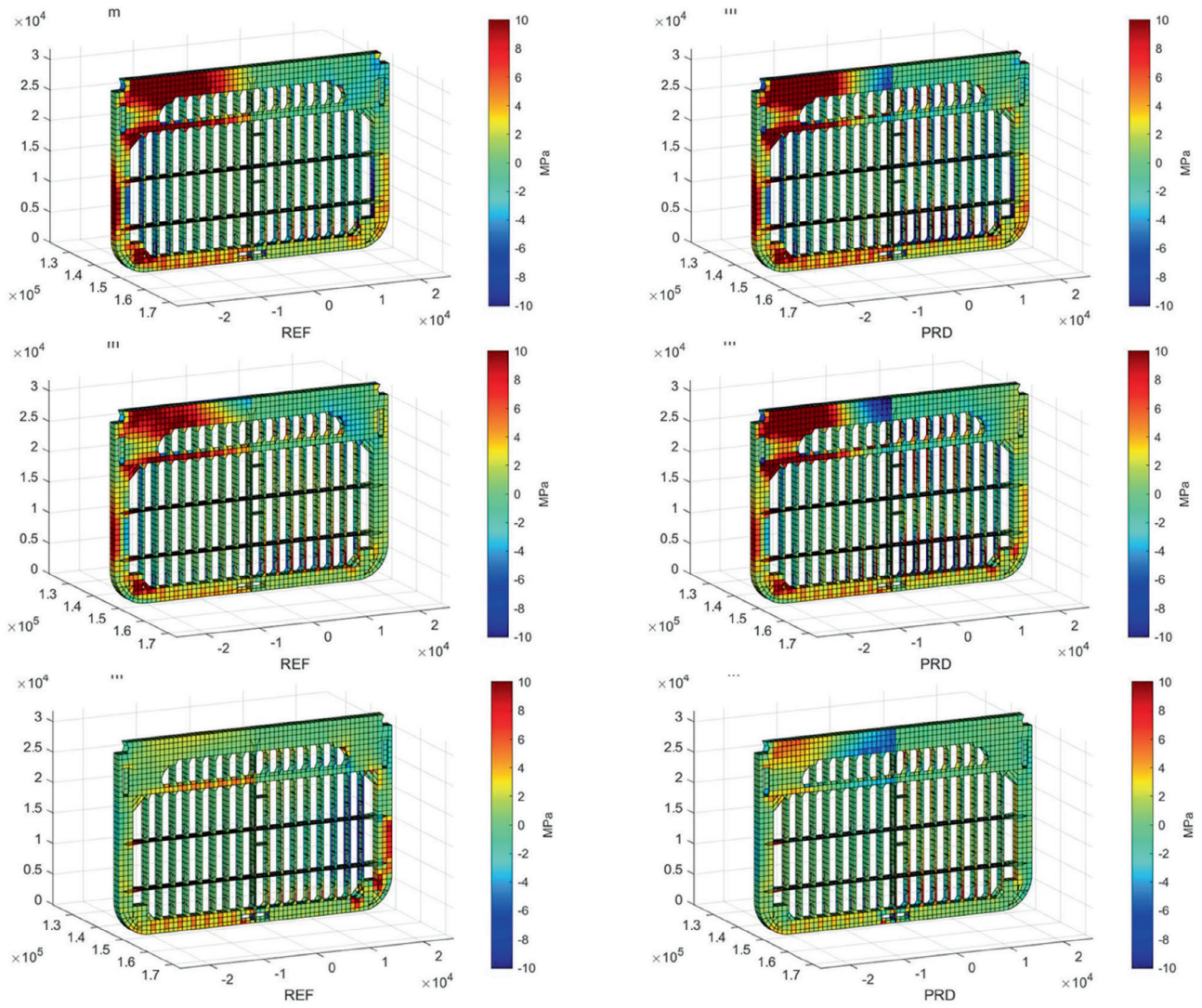

Figure 9. Stress contour plot of non-watertight bulkhead, numerical analysis result (left), and conversion model estimate (right).

estimated and measured time-series stress, power spectral density (PSD), and fatigue damage derived from them. In this study, the time-series stress measured from 18 LBSGs was divided into two groups, one to be used as the input of the conversion model and the other to be compared with the conversion model estimate. The input group consists of a set of measured stress at seventeen LBSGs, and the time-series stress measured at only one LBSG is assigned to the output group. By estimating the stress response of one sensor using the remaining sensors, it is possible to determine whether the sensor in prediction has failed or is being affected by a factor other than global hull structural behaviour.

The prediction of the conversion model is tuned to accurately predict the numerical analysis data used to construct the conversion matrix. If the numerical analysis conditions and the actual ship operating conditions do not exactly match, it is hard to expect the conversion model estimate to match the actual structural response. Although this error would not be very significant, the phase of some estimated structural responses may show some phase difference about a few seconds from the actual one. As would be expected, the size of the estimate may also be different, but there doesn't seem to be any other option to fix this error at this time. The process is named as "Signal synchronisation" and can be seen in the middle of Figure 10. The process requires a conversion matrix and measured time-series stress. More detailed descriptions of the synchronisation process will be presented through Figure 11 and the following paragraphs.

A comparison between the measured and conversion model predicted stress times series is given in Figure 12.

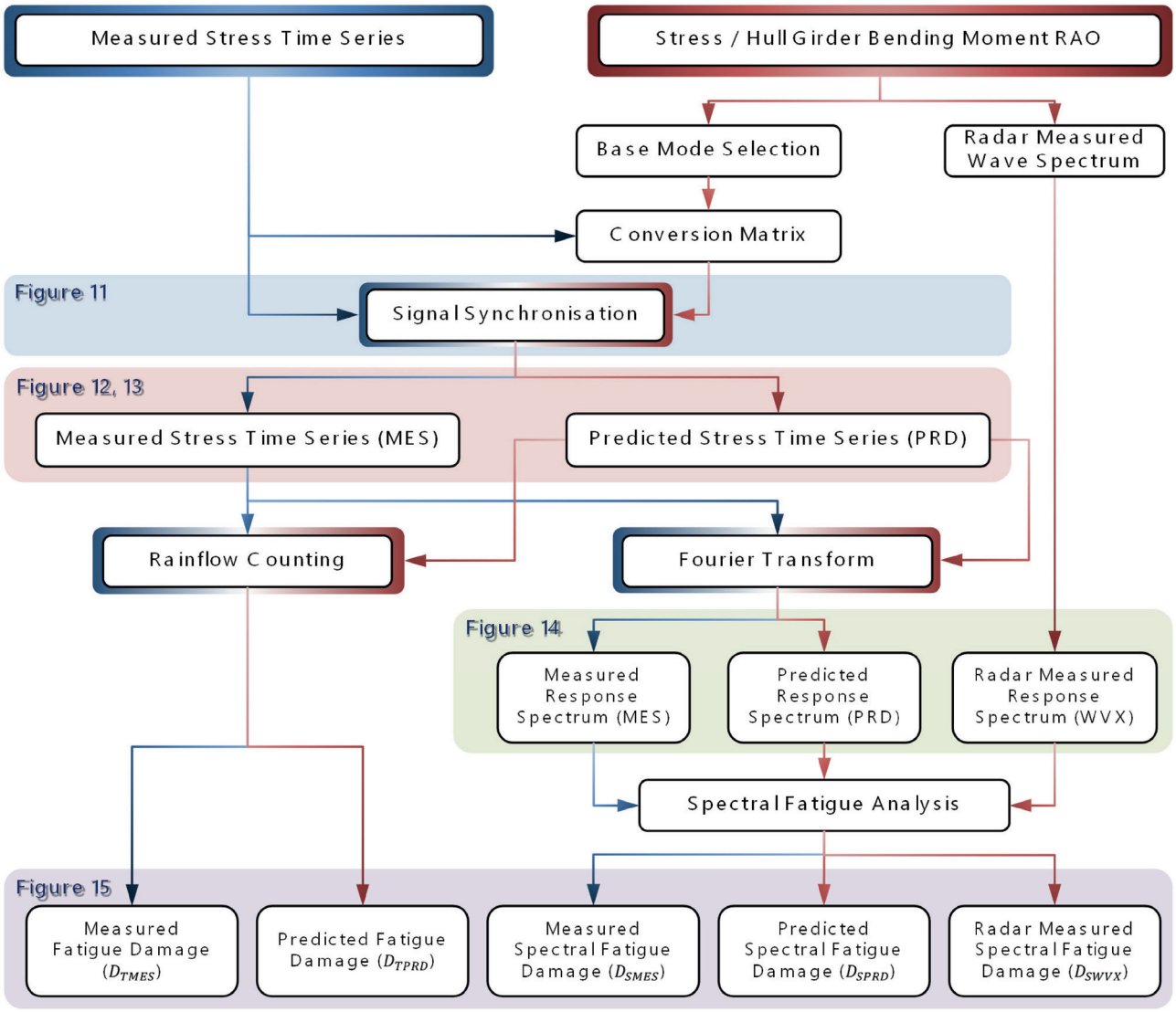

Figure 10. Validation Process using Full Scale Measurement Data.

However, the time series plots can only illustrate the model's accuracy for a short period time. Thus, the time-series stress will be transformed into a response spectrum, and the signal characteristics and model accuracy will be analysed.

Further, once the time-series stress is converted into the spectrum, they can be directly compared with the response spectrum estimated from wave radar measured spectrum. Each type of spectral response plot will be given in Figure 13. Finally, the estimated and measured quantities regarding fatigue damage will be compared, and the results will be presented in Figure 14.

To begin with an explanation of the signal synchronization process, it should be noted that this should not be regarded as a general application of the conversion method. This process is specifically aimed at correcting the loading conditions that were roughly estimated solely through the ship's draft records in Section 4 (and it is worth mentioning that the reliability of that data was highly questionable). In other words, if the actual loading conditions of the ship had been accurately reflected in the numerical model, this process would not have been necessary.

However, given the uncertainty surrounding the loading conditions, failing to attempt the application of the conversion model to full-scale measurement data would be a missed opportunity. For this reason, the process was carried out under the assumption that there would be a phase difference between the estimated structural response time series from the conversion model and the response of the physical ship,

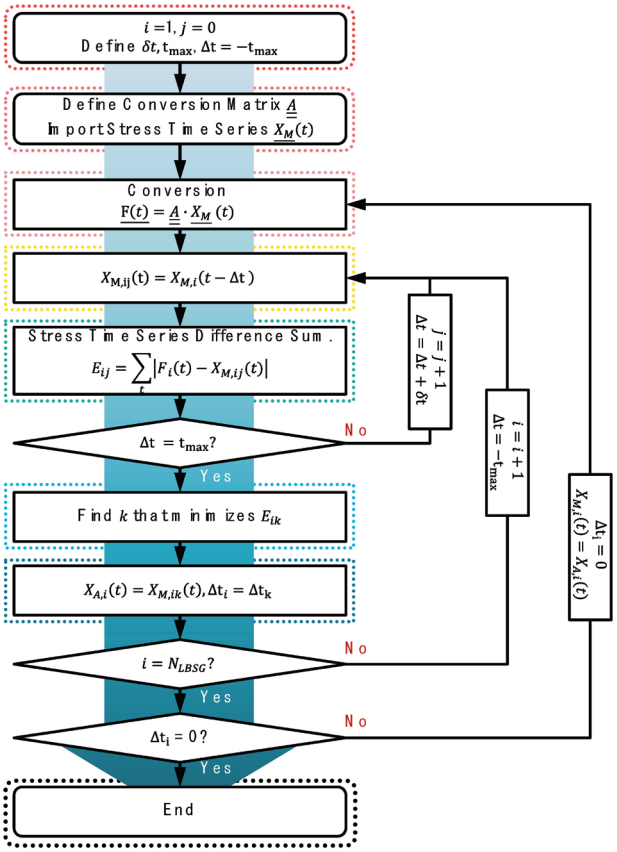

Figure 11. Signal synchronisation process.

and adjustments were made accordingly. Readers with a strict perspective might reasonably criticize this process, as a model intended to explain a phenomenon should not be adjusted based on actual data concerning that phenomenon.

The phase difference between the numerical analysis result and the actual response may be somewhat critical to the predictions from the conversion matrix. The process of producing the conversion model estimates is essentially the same as the process of linearly summing the time-series stress where some constants have been multiplied. Suppose the phase of the signals at each time step is slightly different. In that case, the constructive and destructive interference relation between the input signals may vary during the conversion process, which would increase the error of the estimates as a result. Therefore, before using the LBSG measured stress signal as an input of the conversion matrix, a 'signal synchronising' process was performed to adjust the signal phase.

$$\begin{bmatrix} F_{1,t} \\ F_{2,t} \\ F_{3,t} \\ \vdots \\ F_{18,t} \end{bmatrix} = \begin{bmatrix} 0 & A_{1,2} & A_{1,3} & \cdots & A_{1,18} \\ A_{2,1} & 0 & A_{2,3} & \cdots & A_{2,18} \\ A_{3,1} & A_{3,2} & 0 & \cdots & A_{3,18} \\ \vdots & \vdots & \vdots & \ddots & \vdots \\ A_{18,1} & A_{18,2} & A_{18,3} & \cdots & 0 \end{bmatrix} \cdot \begin{bmatrix} X_{1,t} \\ X_{2,t} \\ X_{3,t} \\ \vdots \\ X_{18,t} \end{bmatrix}$$

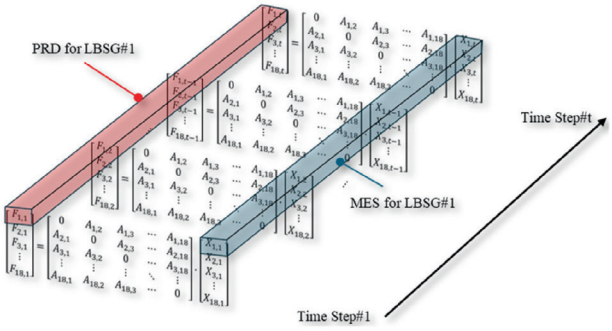

Figure 12. Time-series stress comparison for LBSG 1 through LBSG 3 at time zone 1.

The process shifts the reference stress time signal parallel along the time axis and finds the one best fits the estimated time-series stress among all the shifted signals. On the other hand, this process is not performed only once; accordingly, a multi-loop type method shown in Figure 11 was devised. The shifted time-series stress is again used as the input time-series stress to generate an estimated time-series stress again. The reason why this process is repeated is that the shifted time series changes the estimated time-series stress when they are used as the conversion input. This process is repeated until any more time shifts do not occur. In the end, the shifted time series, which results in the best fit with the estimated time-series stress can be found, and the signal synchronising process is terminated.

Since the conversion matrices transform the 17 input time-series stress into only one prediction signal, the conversion matrix becomes a vector with 17 elements. A new matrix that converts 18 input stress times series into 18 predicted stress signals can be composed by assembling those vectors, as presented in Equation (15). To assemble the conversion matrix $\underline{\underline{A}}$, zeros are padded at the diagonal terms of the matrix, and seventeen elements of each conversion vector to predict the response of the i-th LBSG are assigned at the off-diagonal terms in each row. This reassembled matrix is used as an input of the signal synchronising process, together with the measured time-series stress.

$$\underline{F_t} = \underline{\underline{A}} \cdot \underline{X_t} \tag{15}$$

The iteration number 'i' appearing in the signal synchronisation process diagram corresponds to the identification number of LBSG, thus it has a range from one to eighteen. The iteration number 'j' stands for the number of shifted time steps that occurred in each loop of signal shifting. In the beginning of the synchronisation, the maximum time shift amount t_{max} and step wise time shift amount Δt should be defined. The maximum shift t_{max} was set to be five seconds, and 0.5 seconds to be the step time shift in the application of this process. As a result, the estimation error E_{ij}, the parameter evaluating the time-series stress difference between the estimated stress signal

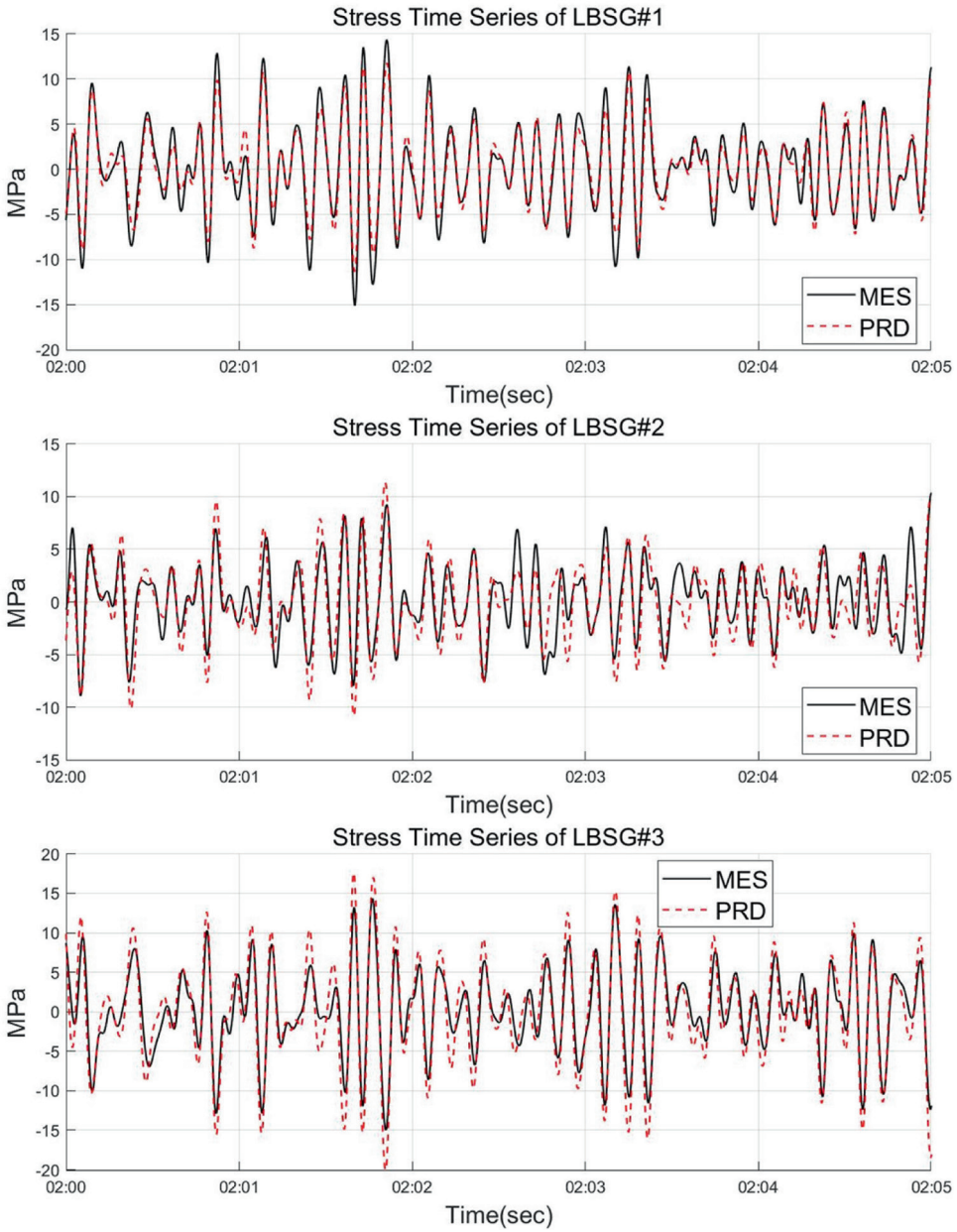

Figure 13. Time-series stress comparison for LBSG 1 through LBSG 3 at time zone 1.

at i-th LBSG for the j times shifted reference stress signal can be calculated. The total amount of the time shift is different for each LBSG, reaching up to 5.5 seconds.

Figure 12 shows both the shifted time-series stress and corresponding predicted stress signals from LBSG 1 through LBSG 3. The black solid line for the 'MES' series corresponds to $X_{i,t}$ from Equation (15), while the red dashed line for the 'PRD' series corresponds to $F_{i,t}$ from the same equation. It might be helpful for viewing the visualised results in Figure 13. Only the results for time zone 1 are illustrated in the figure.

In the numerical analysis process, linear wave loads with a maximum frequency of 1.2rad/s were assumed to compose the conversion matrix. The conversion model may produce untrustworthy estimates for structure response induced by the excitations with shorter periods than the maximum frequency assumed in the analysis stage. Thus, by applying the low pass filter to the time-series stress, the vibrational components with the radial frequency above 1.8rad/s were excluded.

The 'MES' time-series stress of the solid black line in Figure 13 is the LBSG measured time-series stress that has undergone low pass filtering and signal synchronisation. The time-series stress of 'PRD' in the red dotted line is the one generated by applying the conversion matrix $\underline{\underline{A}}$ to the 'MES' type time-series stress. Since the diagonal terms of the conversion matrix are all zero, the predicted signal

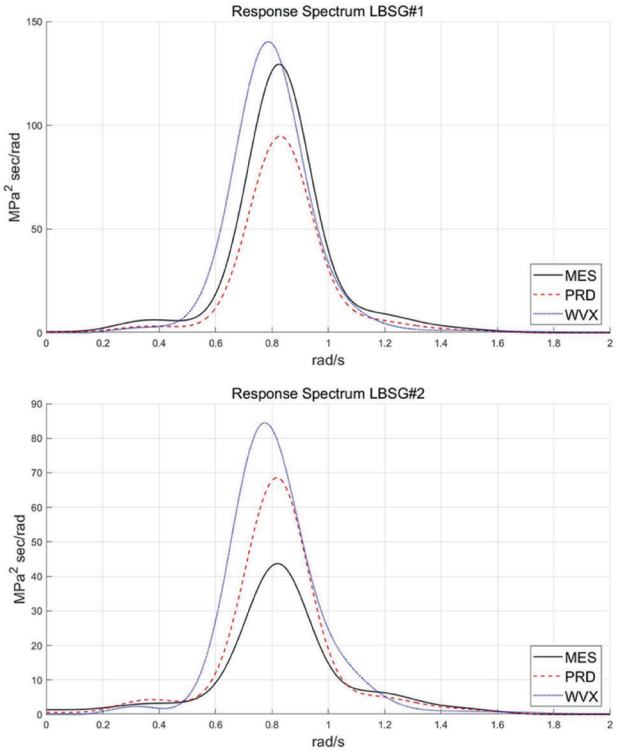

Figure 14. Response spectrums and spectral moments for LBSG 1 (Top) & 2 (Bottom) at time zone 1.

'PRD' for LBSG 1 at the top of Figure 13 is the result estimated from the time-series stress measured at LBSG 2 through 18. It can be seen from the first to the third row of Figure 13 that the two types of time-series stress show a good match. This implies that the estimated structural response from the conversion matrix coincides with the actual structural response of the vessel.

Unfortunately, not all LBSG stress estimates showed accurate results. The estimates for LBSG 1 through 8 located near the midship showed considerable match. However, for LBSG 9 through 12, which are installed right in front of the superstructure of the ship, the estimation accuracy tends to decrease. The conversion model estimate deviated more from the reference for LBSG 13 and 14 installed in the ship front and for LBSG 15 through 18 located in front of the ship engine room.

It seems that, for the bow and stern, this is because the local load conditions near the sensor installation and structural response induced from them pose a more dominant effect on the stress of these areas than the global hull structural behaviour. Furthermore, referring to the arrangement of the sensors, the predictions made in those locations can be seen as spatial extrapolation rather than interpolation, which may have increased the error even more.

The power spectral density (PSD) plots for stress signals of LBSG 1 and 2 are depicted in Figure 14. Since the PSD results contain a stress history of one hour, they illustrate the accuracy of the conversion model estimate for a longer time step than the time-series stress results shown in Figure 13. As the fatigue damage can be estimated from the area and the second moment of the PSD diagram, the utility of the conversion model for structural integrity management can be assessed from these data. The PSD of the 'MES' and 'PRD' series in Figure 14 corresponds to the result of the PSD transformation of the time-series stress of the 'MES' and 'PRD' series, respectively.

The third type of PSD labelled as 'WVX' is also plotted in Figure 14. Multiplying the LBSG stress RAO obtained from the structural analysis by the measured wave spectrum, the stress response spectrum can be obtained, and this is the 'WVX' PSD. The hindcast wave spectrum is used in the full stochastic fatigue analysis process during the ship design stage. The fatigue damage estimates calculated from the hindcast wave spectrum cannot be more accurate than those estimated from the measured wave spectrum. Thus, the estimates derived from the 'WVX' type spectrum indicate the most accurate estimates possibly obtained from the design stage. Otherwise, they can also be interpreted as an indicator implying how close the numerical analysis results are to the actual structural response of the vessel in physical space.

The WVX PSD of LBSG 1 illustrated in Figure 14 seems closer to the REF series than the PRD series. On the other hand, the results for LBSG 2 show the opposite tendency. Though the PSD results for the remaining 16 LBSGs were not attached to this paper, most of the PRD series results are closer to those of the REF series than the WVX series. This seems to be due to the advantage that the conversion method considers only the actual hull structural behaviour during the operation. However, as can be seen in cases such as LBSG 1, where there are noticeable differences in PSD, further research is required to account for the uncertainties associated with the estimated stresses.

Figure 15 summarises the fatigue damage ratio results calculated from rainflow counting and spectral fatigue analysis method at 18 LBSG locations. For rainflow counting and power spectral density analysis, version 2017 of the open-source MATLAB code package Wave Analysis for Fatigue and Oceanography (WAFO) was utilised. The stress cycles were counted according to ASTM E1049-85 (2017) standard. The S-N curve for the welded joints with cathodic protection (16) in DNV classification note 30.7 (DNVGL, 2014) was used to evaluate the estimation accuracy of the conversion model from the fatigue damage. It would be appropriate to compare the model accuracy for stress concentrations where fatigue damage may occur within the lifetime of the vessel. However, there is no time-series stress measured at those locations. Therefore, although fatigue damage is unlikely to occur, the fatigue damage ratios of LBSG locations where time-series stress were measured were calculated.

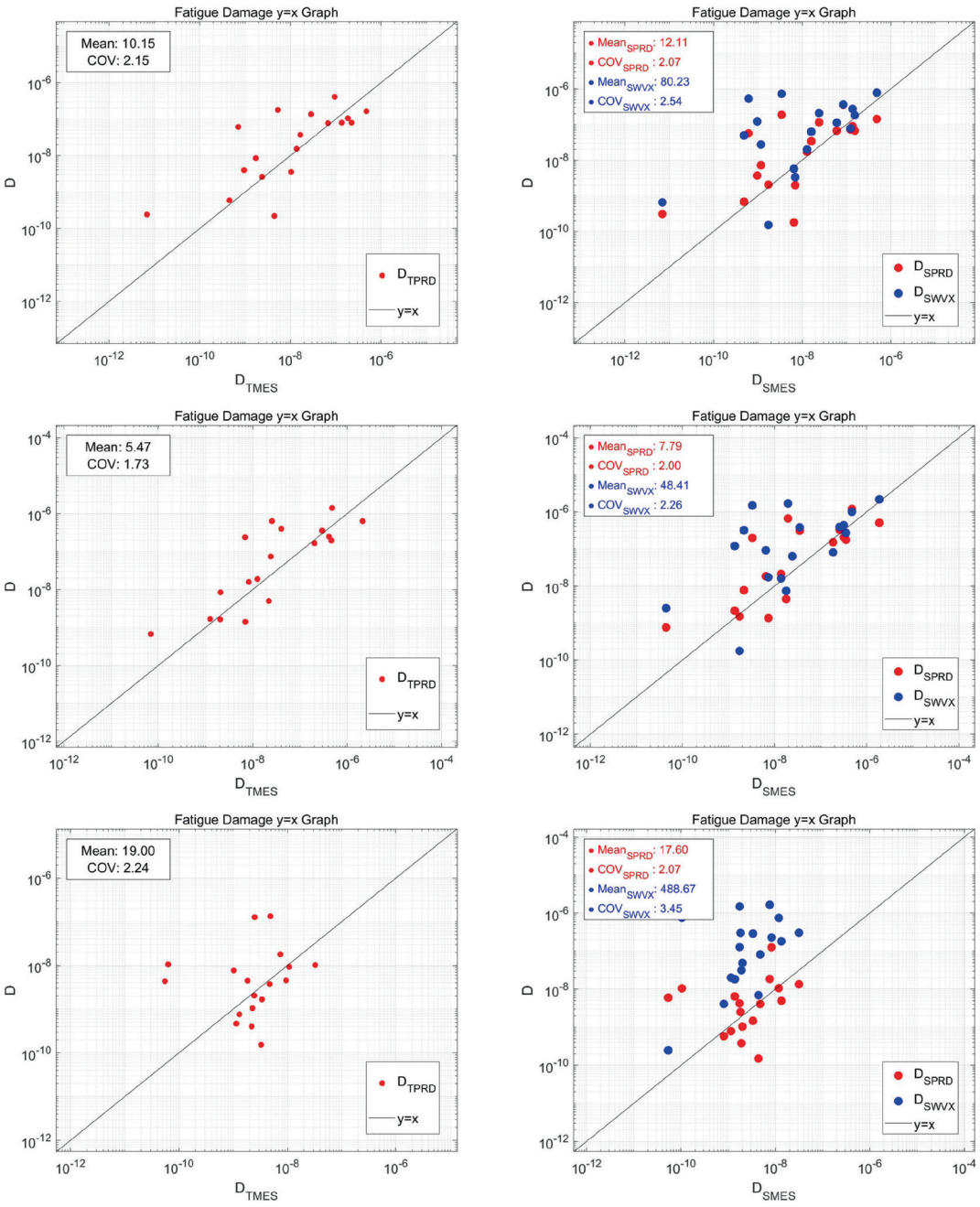

Figure 15. Fatigue damage ratio for each LBSG location calculated by rainflow counting method (Left) and spectral fatigue analysis procedure (Right) for time zone 1.

$$\log N = \log \bar{a} - m \log K_p \Delta\sigma \quad (16)$$

K_p: Stress reduction factor, 0.72

$\bar{a}$: SN-Curve property, 15.606

m: SN-Curve property, 5.0

The LBSGs are installed on the longitudinal stiffeners. For the calculation of the fatigue life or strength, S-N curve type I (Welded joint) from the DNV No. 30.7 (DNVGL, 2014) has been utilised, and the detailed can be referred to Appendix B (Table B.1 and Figure B.1). In the event that the principal stress direction is parallel with the weld direction, it is necessary to apply a stress reduction factor (K_p) to the principal stress range prior to entering the stress value into the S-N curve (DNVGL, 2014). The value of the stress reduction factor was determined on the assumption that automatic welding was conducted on both sides (K_p = 0.72) which is clearly stated in Table A.2. Since the maximum change in amplitude of the time-series stress is lower than the fatigue limit of 73.1Mpa, the S-N curve for $N \geq 10^7$ was used.

The relation between fatigue damage and the spectral moment is as written in Equation (17). The 'D' is the

fatigue damage to be calculated, and T_d is the length of time for which the time-series stress was measured. Here, T_d was set to be 3600 seconds since the time-series stress was measured for an hour. The K_p, $\bar{a}$, and m are values obtainable from the S-N curve. The value obtained by integrating the response spectrum in the previous section was used for the spectral moment.

$$D = \frac{T_d}{2\pi\left(K_p^{-m}\bar{a}\right)}\sqrt{\frac{m_2}{m_0}}\left(2\sqrt{2m_0}\right)^m \Gamma\left(1+\frac{m}{2}\right) \quad (17)$$

D: Fatigue damage ratio

T_d: Design Life, 3600sec (Stress measured time length)

m_0: Spectral moment, $\int_0^\infty S_R(\omega)\,d\omega$

m_2: Spectral moment, $\int_0^\infty \omega^2 S_R(\omega)\,d\omega$

Figure 15 shows the two types of fatigue damage, one calculated from rainflow counting the time-series stress, and the other from the spectral fatigue analysis method. Fatigue damage calculated directly from the time-series stress is denoted with a 'T' subscript, and D_{TMES} and D_{TPRD} are of this case. D_{TMES} and D_{TPRD} are the fatigue damage calculated by rainflow counting the measured and estimated time-series stress, respectively. The fatigue damage determined by applying the spectral fatigue analysis procedure to the response spectrum obtained from the measured and the estimated time-series stress was denoted as D_{SMES} and D_{SPRD} using the 'S' subscript. The fatigue damage calculated from the wave spectrum measured by WAVEX is written as D_{SWVX}.

Figure 15 consists of scatter diagrams arranged in three rows and two columns. Each row contains the fatigue damage calculation results for time zone 1, 2 and 3. The X-coordinates of the data points in the left plots of the figure denote D_{TMES} for each LBSG. The X coordinates of the data points in the plots on the opposite side represent D_{SMES}. The estimated time-series stress is calculated for each of the 18 LBSGs, which results in 18 data points per graph. Mean and COV (coefficient of variation) are provided to compare the estimated results. As the Red dots in the graphs on the left are densely clustered around the diagonals, it can be inferred that the fatigue damages were accurately estimated from the conversion model even for the longer time-series stress measured for an hour length. On the other hand, the results for time zone 3 in the third row show a more dispersed distribution than it is for the results in the first and second rows. Compared to other time zones, the loading condition of the ship in the time zone 3 is more different from the one assumed in the numerical analysis, and it seems to be the cause of the accuracy deterioration of the conversion method in this time zone.

In the graphs on the right, the D_{SPRD} series data points are more closely gathered around the y = x line than the D_{SWVX} series are. This is consistent with the result illustrated from the PSD plot, which means that the conversion method that accounts for the actual response of the hull structure in the prediction process produces fewer errors than the one estimated from the wave spectrum, in other words, the design estimates. This is more clearly shown in the results for time zone 3. Whereas the D_{SWVX} series fully contains the error from the numerical analysis results, the error of the D_{SPRD} series is diminished since the conversion model estimates vary along with the conversion model input changes. The reason why the D_{SWVX} series are closer to the diagonal than the series can be explained as above.

7. ADDITIONAL EXAMPLE FOR USER GUIDE

The method described in this study does not necessarily apply to the 13,00 TEU container ship but can also be applied to many other vessels with different hull structures. To clarify this point and provide a comparison model for cross-validation that can proceed later, an additional working example of a relatively simpler model is introduced in the following.

The new target vessel is a FPSO model, as illustrated in Figure 16, and its principle dimensions are shown in Table 3. The vessel is the sample FPSO model, which is an analysis example provided in the Sesam software package. The hydrodynamic and structural analysis and post-processing for the sample FPSO model were conducted using version 2013 of the Sesam software package.

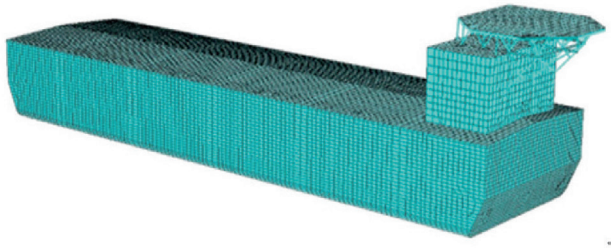

Figure 16. SE-23 FPSO model (Sample model)

Table 3. Principle dimensions of FPSO

Light weight	15,000ton
Dead weight	111,170ton
LBP	165.75m
Breadth	43m
Depth	22m
Draft	15.5m

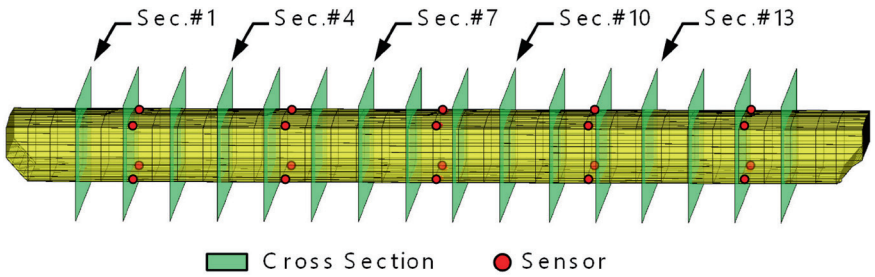

Figure 17. Load cross-section and sensor locations of FPSO.

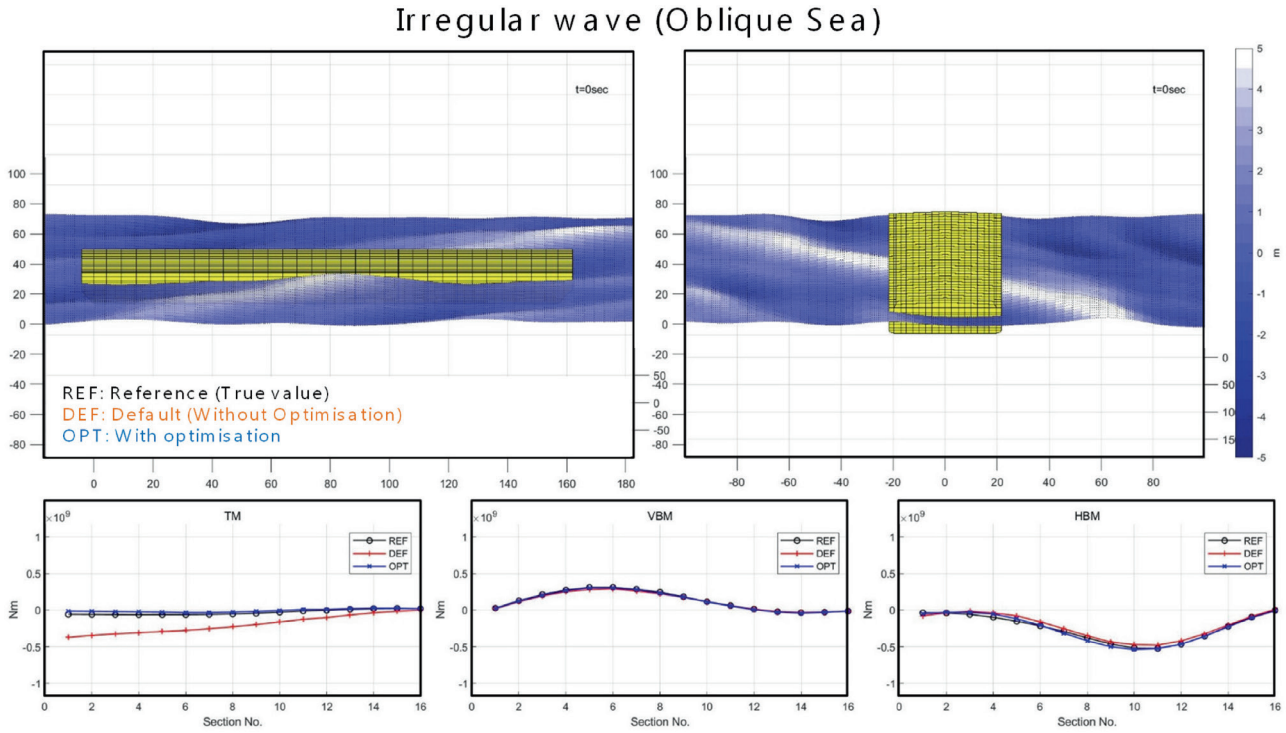

Figure 18. Comparison of hull girder moment distribution in irregular oblique sea wave for FPSO.

The hull girder bending moments were calculated across sixteen load cross sections, as illustrated in Figure 17, for comparison with the conversion model estimates. For the conversion model input, membrane stress components in the global x-direction at twenty shell elements across five (5) transverse sections were taken, and the locations are marked in red point in Figure 17.

The comparison between the analysis result and the conversion model estimates for the hull girder moment is shown in Figure 18. The sea state of wave heading 120 degrees, significant wave height of 10 metres and peak period of 10 seconds was assumed using the Pierson-Moskowitz modified spectrum. Both of the conversion models yield accurate estimates for the vertical and horizontal bending moments. However, it is confirmed that the conversion model set up based on the 'OPT' case selection method provides the most accurate results for the torsional moment. This is similar to what has been demonstrated in the 13,000TEU container ship application.

Figure 19 demonstrates the analysis result and conversion model estimates for the web frame membrane stress. Among the total of 30 web frames comprising the hull structure, the 15th one from the bow near the midship section was selected for comparison. The stress of 448 nodes on the web frame was directly calculated from the multiplication of 20 stress input values and the conversion matrix. The same sea state as the hull girder bending moment example was assumed. The contours in the first

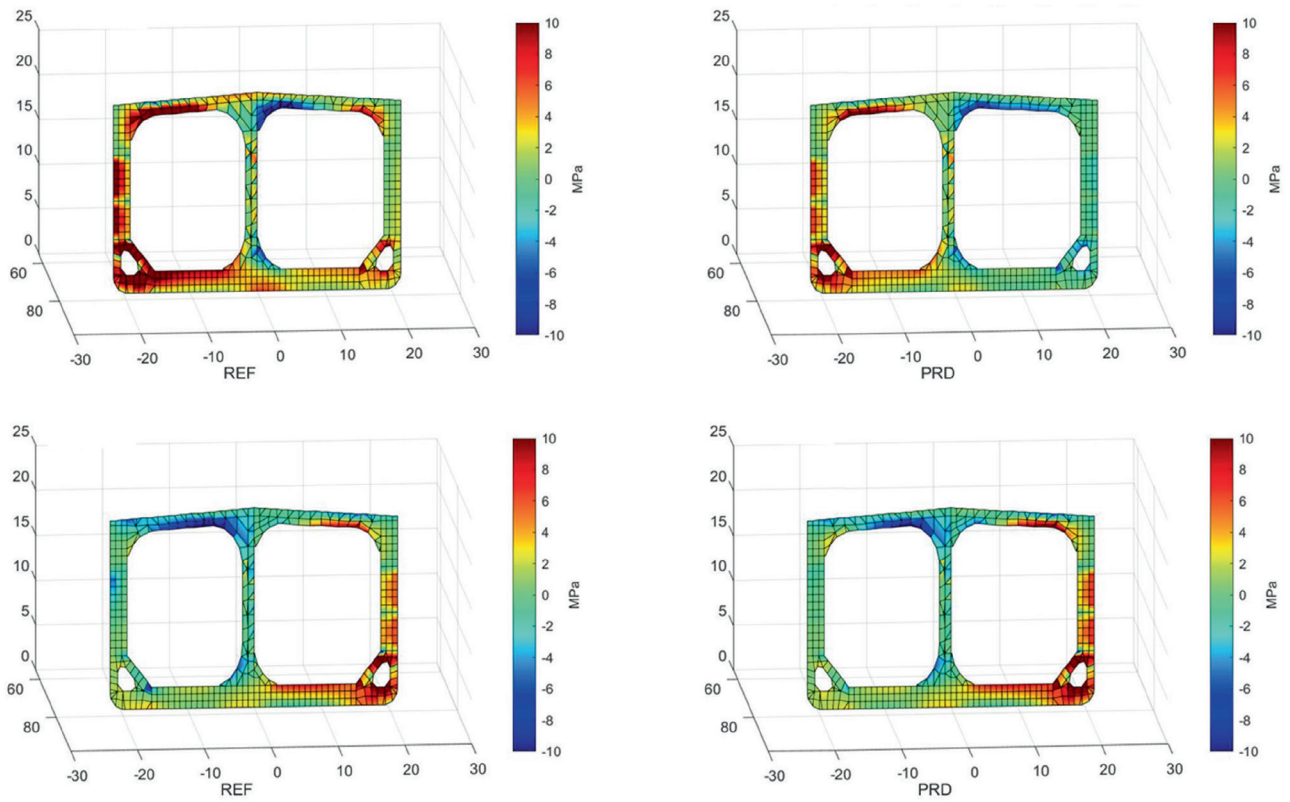

Figure 19. Stress contour plot of FPSO web frame, numerical analysis result (left), and conversion model estimate (right)

row in Figure 18 demonstrate the results at the simulation time of 30 seconds, and the 2nd row includes the results at 40 seconds.

In Figure 19, the contours in the left column show the web frame stress obtained from the analysis and the right column contains the estimates from the conversion model. It can be seen in Figure # that the conversion model estimates show stress contours of similar patterns and magnitudes to the ones from the analysis result. Considering the results presented through Container ship and the FPSO examples, the conversion model with the optimised base mode selection algorithm is expected to provide more accurate estimates compared to the one with the default mode selection method.

The conversion model has not been extensively tested on a wide range of offshore structures. Therefore, further research is needed to understand better the types of structures to which this approach can be applied and its applicability. In this paper, the conversion model has been applied to barge-type FPSOs and container ships. Further research is needed to explore the application to a wider range of structure types, including floating offshore wind turbines.

It has been found that this method is useful in estimating the global structural response of these models. Therefore, users of this model should be cautious and apply the methodology specifically to cases where the structural response they wish to estimate is driven by global hull structural deflections that can be decomposed into modal shapes. Further research is required to improve the estimation accuracy in areas where the influence of local hydrodynamic pressure is significant.

Large container ships are subject to high-frequency vibration caused by whipping, which is a significant contributor to fatigue damage. The frequency of the wave load cases used to construct the conversion model in this study consists mainly of low-frequency components not exceeding 1.1 rad/s. Therefore, it is unlikely that the conversion model can accurately estimate the structural response of the hull to high-frequency vibration. Further research into the ability of the conversion model to handle high-frequency vibration components would be beneficial.

8. CONCLUSIONS

This study aims to enhance the conversion matrix used for predicting loads at arbitrary locations based on limited stress measurements. An optimised base mode selection method was proposed to improve the accuracy of the conversion matrix, which was calculated using mode superposition. When selecting modes using responses to

regular waves, the initial mode and the number of modes play a critical role. In this paper, we sought to refine the mode selection process by identifying the combination that minimises error compared to numerical analysis results. The proposed mode selection method was validated using actual measurement data from the 13,000TEU class container ship, confirming that it offers better estimations than previous approaches. Further validation was performed with an FPSO.

However, a limitation of this study is that the validation focused only on stress estimation and fatigue damage assessment. For implementing the digital twin, additional evaluations should include real-time buckling assessments to ensure structural integrity monitoring. Furthermore, while the effectiveness of the optimization introduced in the mode selection process has been confirmed to a limited extent within the scope of this study, additional research is needed to ascertain whether it constitutes a clear improvement over the methods of other authors.

In addition, estimating high-frequency regimes affected by whipping and springing also requires further validation. This method assumes that the analysis results in the elastic range are represented by modal superposition, which means it cannot predict any plastic deformation. Since plastic deformation occurs in the hull and significantly impacts structural integrity, further research shall be conducted to develop advanced models to address this issue.

9. ACKNOWLEDGEMENTS

Some part of the present research is a result of a research project, "Development of Hull Integrity Management System based on Digital Twin Technology", supported by Daewoo Shipbuilding and Maritime Engineering Co. Ltd., Hyundai Heavy Industries Co. Ltd, Korean Register and KRISO. This research has also been supported by the MOTIE (Ministry of Trade, Industry, and Energy) in Korea, under the Fostering Global Talents for Innovative Growth Program (P0008747) supervised by the Korea Institute for Advancement of Technology (KIAT). All support is gratefully acknowledged. In this manuscript, some figures, i.e., 7-9, 12-14, 18 and 19, were generated using MATLAB version 2020b. Some of this study summarises Mr. D.Y. Lee (1st author)'s MSc thesis (Lee, 2022), supervised by Prof. B.S. Jang and titled "Hull Structural Response Prediction using Distortion Base Modes" from the Seoul National University, Korea. Some parts of the study have also been presented at the MARSTRUCT2021 conference.

10. REFERENCES

1. ABIDEEN, A Z., SUNDRAM, V P K., PYEMAN, J., OTHMAN, A K. and SOROOSHIAN, S. (2021). *Digital Twin Integrated Reinforced Learning in Supply Chain and Logistics*. Logistics. 5: 84 (https://doi.org/10.3390/logistics5040084).
2. ANDONIU, A., LAUZON, J. and LAMAISON, V. (2019). *Full Scale Measurements of the Hydro-Elastic Behavior of A 13000 Teus Container Ship*. Trends in the Analysis and Design of Marine Structures – Parunov & Guedes Soares (Eds), CRC Press, London, UK (9780429298875).
3. ASTM (2017). *Standard Practices for Cycle Counting in Fatigue Analysis (E1049-85)*. ASTM International, West Conshohocken, PA, USA.
4. BAUDIN, E., BIGOT, F., DERBANNE, Q., SIRETA, F X. and QUINTON, E. (2013). *Increasing ULCS Structural Response Knowledge Through 3D FEM and a Comprehensive Full-Scale Measurement System*. The 23rd International Offshore and Polar Engineering Conference (ISOPE 2013), Anchorange, Alaska, USA, June 30 – July 5 (ISOPE-I-13-646).
5. BIGOT, F., DERBANNE, Q. and BAUDIN, E. (2013). *A Review of Strains to Internal Loads Conversion Methods in Full Scale Measurements*. The 12th International Symposium on Practical Design of Ships and Other Floating Structures (PRADS 2013), Changwon, Korea, October 20-25.
6. BIGOT, F., SIRETA, F.X., BAUDIN, E., DERBANNE, Q., TIPHINE, E. and MALENICA, S. (2015). *A novel solution to compute stress time series in nonlinear hydro-structure simulations*. The 34th International Conference on Ocean, Offshore and Arctic Engineering (OMAE2015), St. John's, Newfoundland, Canada, May 31 – June 5 (OMAE2015-42014).
7. CHEN, B.-Q., LIU, K., YU, T. and LI, R. (2024). *Enhancing Reliability in Floating Offshore Wind Turbines through Digital Twin Technology: A Comprehensive Review*. Energies. 17(8): 1964 (https://doi.org/10.3390/en17081964).
8. DNVGL. (2021). Fatigue Assessment of Ship Structures. DNVGL-CG-0129. Oslo, Norway.
9. DNVGL. (2014). Classification Notes No. 30.7 Fatigue Assessment of Ship Structures. Oslo, Norway.
10. MOKHTARI, K E., PANUSHEV, I. and McARTHUR, J.J. (2022). *Development of a cognitive digital twin for building management and operations*. Frontiers in Built Environment. 8: 856873 (https://doi.org/10.3389/fbuil.2022.856873).
11. FUJIKUBO, M., OKADA, T., MURAYAMA, H., HOUTANI, H., OSAWA, N., IIJIMA, K., HAMADA, K., TOH, K., OKA, M., HIRAKAWA, S., SHIBATA, K., ASHIDA, T., ARIMA, T., TANAKA, Y., TATSUMI, A., TAKEUCHI, T., MITSUYUKI, T., MIKAMI, K., KOBAYASHI, M., KOMORIYAMA, Y., MA, C., CHEN, X., OCHI, H. and MIRATSU, R. (2024). *A digital twin for ship structures - R&D project in Japan*. Data-Centric Engineering. 5: e7 (https://doi.org/10.1017/dce.2024.3).

12. SONG, H., YANG, G., LI, H., ZHANG, T. and JIANG A. (2023). *Digital twin enhanced BIM to shape full life cycle digital transformation for bridge engineering.* Automation in Construction. 147: 104736 (https://doi.org/10.1016/j.autcon.2022.104736).
13. JONES, D., SNIDER, C., NASSEHI, A., YON, J. and HICKS, B. (2020). *Characterising the Digital Twin: A systematic literature review.* CIRP Journal of Manufacturing Science and Technology. 29(Part A): 36–52 (https://doi.org/10.1016/j.cirpj.2020.02.002).
14. KEFAL, A. and OTERKUS, E. (2015). *Structural health monitoring of marine structures by using inverse finite element method*. The 5th International Conference on Marine Structures (MARSTRUCT 2015), Southapton, UK, March 27-27.
15. KEFAL, A. and OTERKUS, E. (2016). *Displacement and stress monitoring of a Panamax containership using inverse finite element method*. Ocean Engineering. 119: 16–29 (https://doi.org/10.1016/j.oceaneng.2016.04.025).
16. KONING, J. and SCHIERE, M. (2014). *Measuring hull girder deformations on a 9300 TEU containership*. International Journal of Naval Architecture and Ocean Engineering. 6: 1111–1129 (https://doi.org/10.2478/IJNAOE-2013-0234).
17. KOBAYASHI, M., JUMONJI, T. and MURAYAMA, H. (2019). *Three-dimensional Shape Sensing by Inverse Finite Element Method based on distributed Fiber-optic Sensors*. The 14th International Symposium on Practical Design of Ships and Other Floating Structures (PRADS 2019), Yokohama, Japan, September 22-26.
18. LATTANZI, L., RAFFAELI, R., PERUZZINI, M. and PELLICCIARI, M. (2021). *Digital twin for smart manufacturing: a review of concepts towards a practical industrial implementation.* International Journal of Computer Integrated Manufacturing. 34(6): 567–597 (https://doi.org/10.1080/0951192X.2021.1911003).
19. L'HOSTIS, D., LECH, M. and AALBERTS, P. (2010). *Overview of the Monitas JIP*. The 41st Offshore Technology Conference (OTC 2010), Houston, Texas, USA, May 3-6 (OTC 20871).
20. LI, S. and BRENNAN, F. (2024a). *Digital twin enabled structural integrity management: Critical review and framework development*. Proc. of the Institution of Mechanical Engineers, Part M: Journal of Engineering for the Maritime Environment. 238(4): 707–727 (https://doi.org/10.1177/14750902241227254).
21. LI, S. and BRENNAN, F. (2024b). *Implementation of digital twin-enabled virtually monitored data in inspection planning*. Applied Ocean Research, 144, 103903 (https://doi.org/10.1016/j.apor.2024.103903).
22. LIU, M., FANG, S., DONG, H. and XU, C. (2021). *Review of digital twin about concepts, technologies, and industrial applications.* Journal of Manufacturing Systems 58: 346–361 (https://doi.org/10.1016/j.jmsy.2020.06.017).
23. MathWorks. (2024). MATLAB. [Computer software]. Available at: https://www.mathworks.com
24. PENROSE, R. (1956). *On best approximate solutions of linear matrix equations*. Mathematical Proceedings of the Cambridge Philosophical Society. 52(1): 17–19 (https://doi.org/10.1017/S0305004100030929).
25. PHANDEN, R.K., SHARMA, P. and DUBEY, A. (2021). *A review on simulation in digital twin for aerospace, manufacturing and robotics*. Materials Today: Proceedings. 38(Part 1): 174–178 (https://doi.org/10.1016/j.matpr.2020.06.446).
26. Shen, M., and GAO, Q. (2019). *A review on battery management system from the modeling efforts to its multiapplication and integration.* International Journal of Energy Research. 43: 5042–5075 (https://doi.org/10.1002/er.4433).
27. SONG, S W, JIN, C. and KIM, D K., *A novel approach for ship digital twin optimisation: principal component analysis-driven distortion base mode selection and utilisation*, The 43rd International Conference on Ocean, Offshore and Arctic Engineering (OMAE2024), Singapore, Singapore, June 9-14 (OMAE2024-124226).
28. SINDI, A., KIM, H.J., YANG, Y J., THOMAS, G. and PAIK, J K. (2024). *Advancing digital healthcare engineering for aging ships and offshore structures: an in-depth review and feasibility analysis*. Data-Centric Engineering. 5: e18 (https://doi.org/10.1017/dce.2024.14).
29. SUGIMURA, T. and MATSUMOTO, S. (2021). *Hull Condition Monitoring and Lifetime Estimation by the Combination of On-Board Sensing and Digital Twin Technology*. The 52nd Offshore Technology Conference (OTC 2021), Virtual and Houston, Texas, USA, August 16-19 (OTC-30977-MS).

APPENDIX A

The additional validation results are illustrated in the appendix by adopting four scenario cases with video links.

Figure A.1(a) shows the regular wave simulation result for the head sea condition. In the following plots, the sign convention of the hull vertical bending moment under the hogging and sagging condition is reversed to ease the comparison between the hull girder moment profile and surrounding wave configuration. The corresponding results for the oblique wave condition are illustrated in Figure A.1(b). The HBM result for the oblique wave case reveals that more accurate estimates are produced in the order of SEP, OPT, and DEF cases, which clearly shows the effect of optimisation.

The results for the irregular sea wave condition are included in Figure A.2. The head sea condition is assumed for Figure A.2(a), and it can be seen in the plots for the TM and HBM that the estimation accuracy is enhanced as a result of the optimisation. The same can be inferred from TM and HBM plots in Figure A.2(b), which demonstrates the estimation results under the oblique sea wave condition.

All the validation video materials are also available at the link given, and they may support potential readers' better understanding.

Regular wave

– Case 1: Head sea condition
(https://youtu.be/YJeTQ1BsQkc)
– Case 2: Oblique sea condition
(https://youtu.be/0rlQRcRR6kY)

Irregular wave

– Case 3: Head sea condition
(https://youtu.be/7u8EZOlqcsM)
– Case 4: Oblique sea condition
(https://youtu.be/e8uIlXfVmlQ)

The additional validation results are illustrated in Appendix A in total of seven figures and video links.

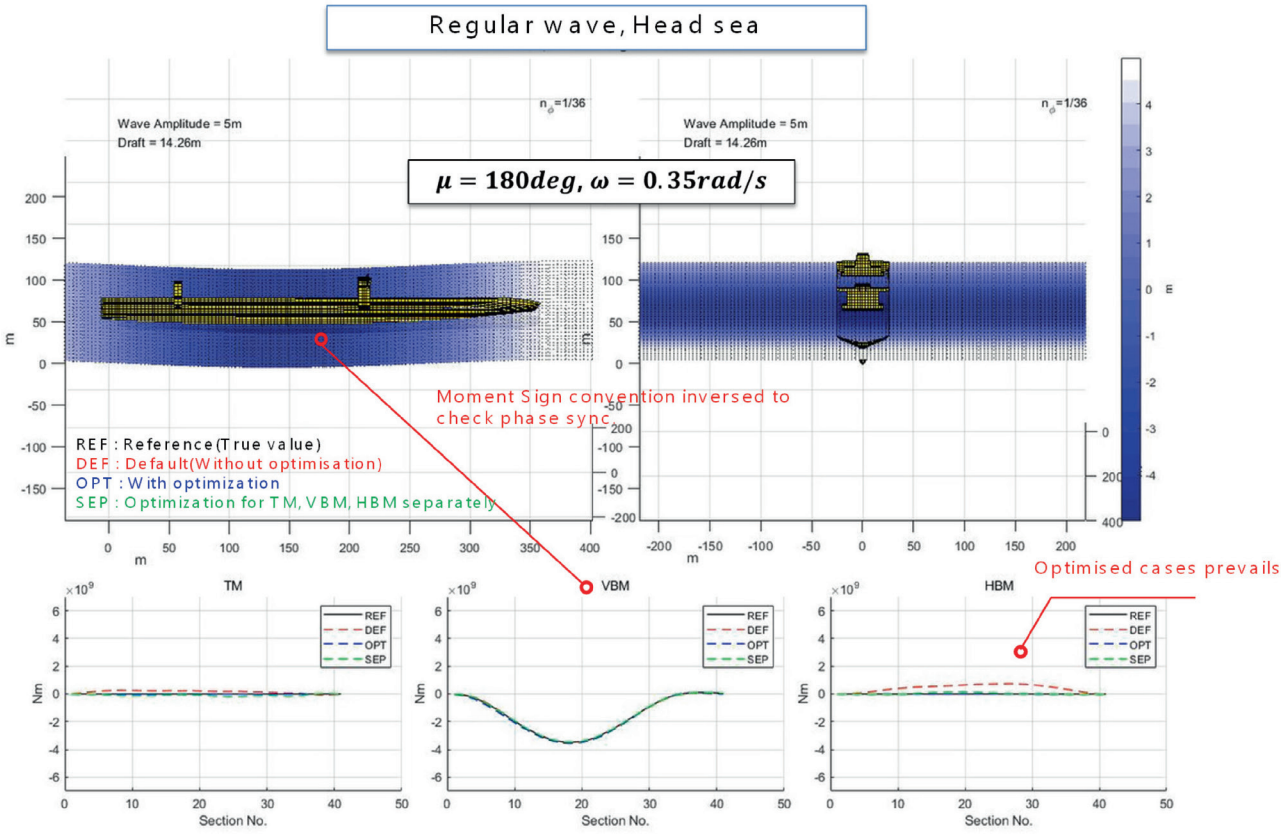

(a). Case 1: Head sea condition ($\mu = 180deg$, $\omega = 0.35rad/s$) (Link: https://youtu.be/YJeTQ1BsQkc)

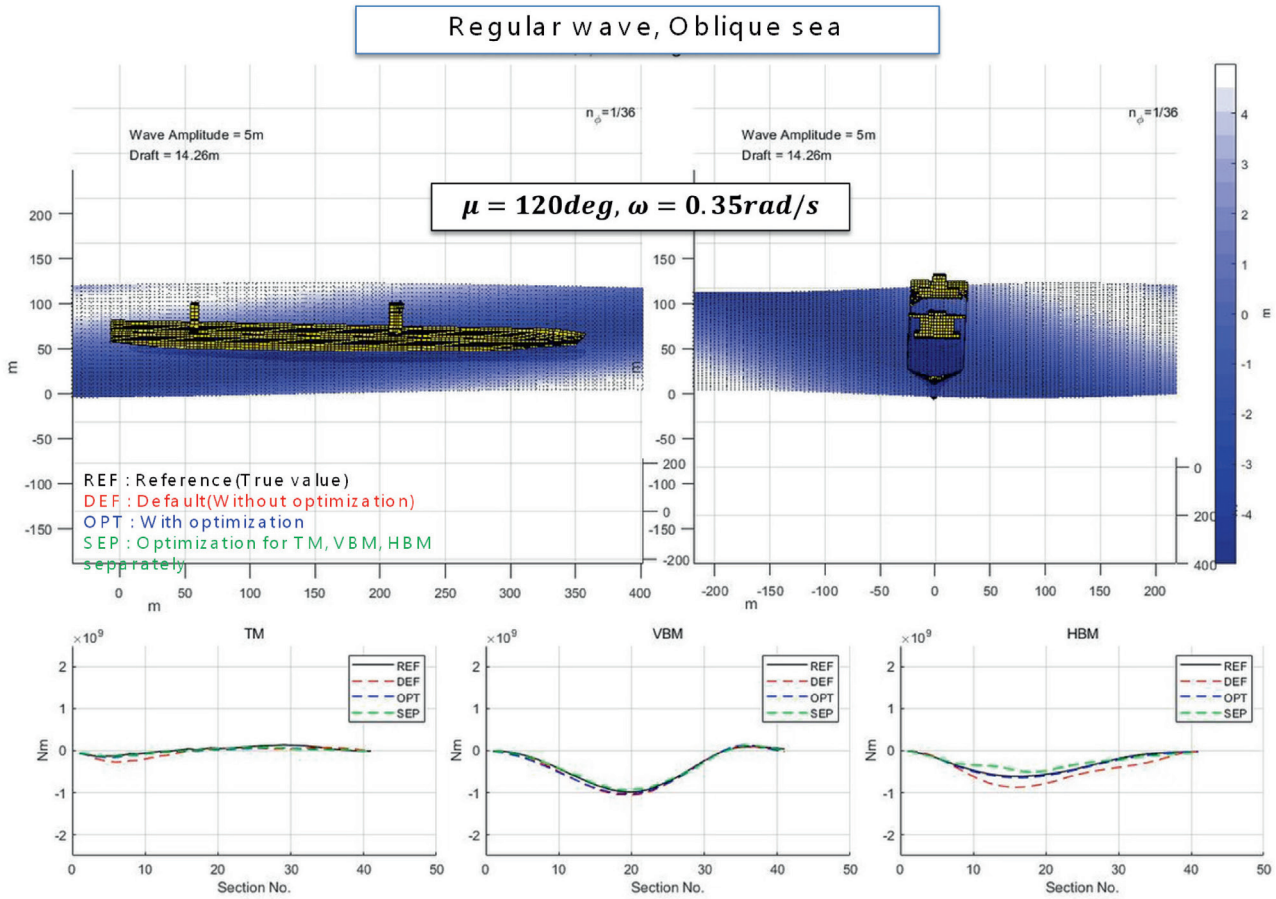

(b). Case 2: Oblique sea condition (μ = 120*deg*, ω = 0.35*rad/s*) (Link: https://youtu.be/0rlQRcRR6kY)

Figure A.1: Validation results under regular waves

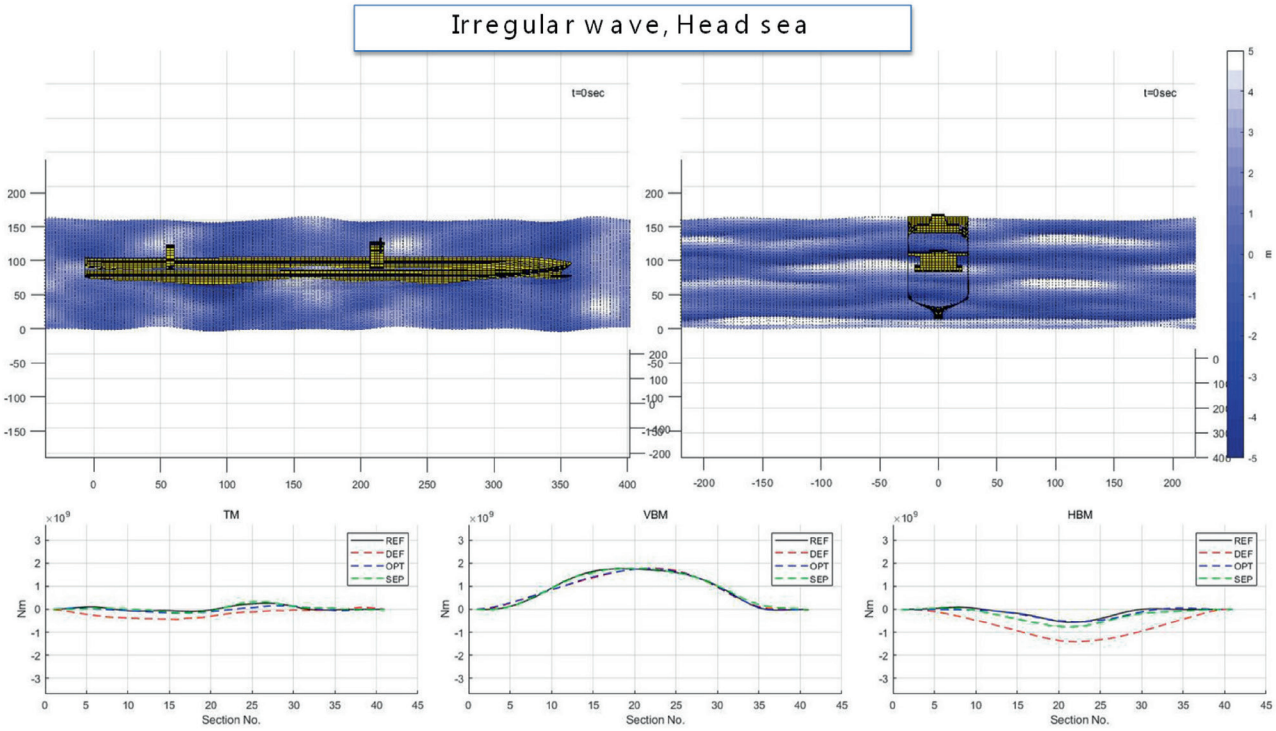

(a). Case 3: Head sea condition (Link: https://youtu.be/7u8EZOlqcsM)

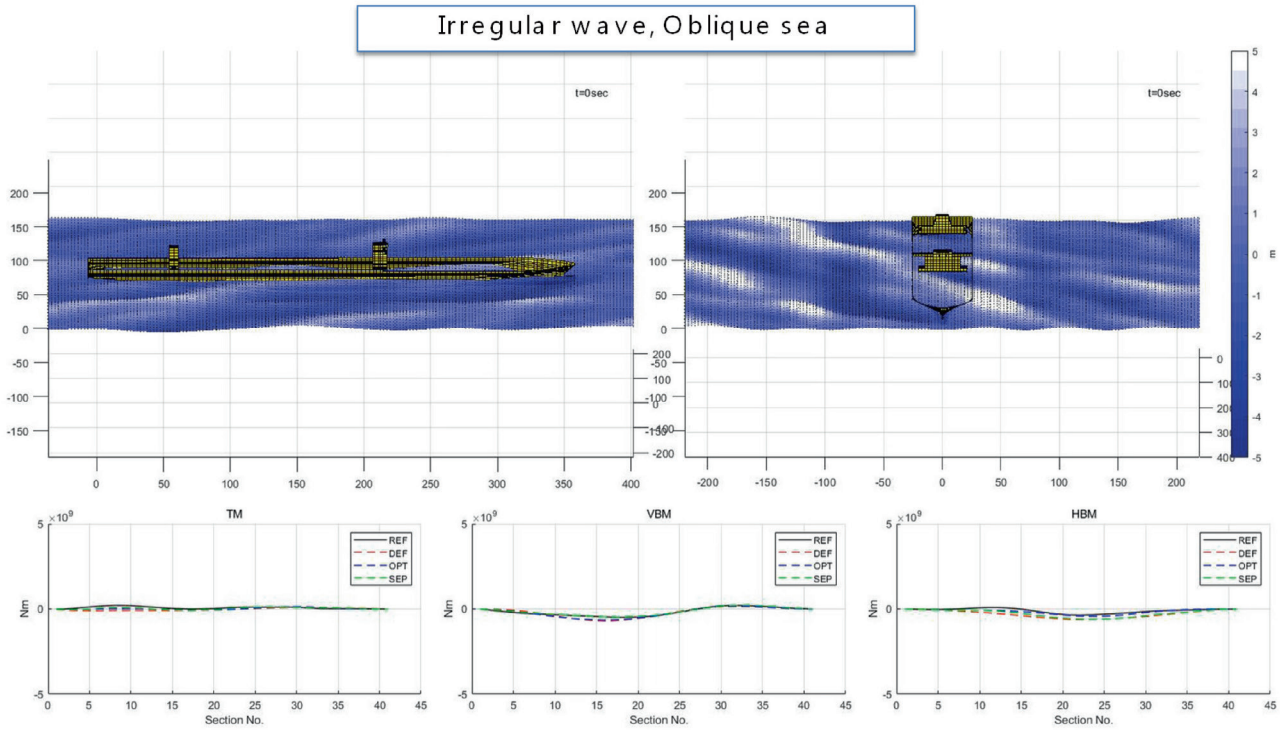

(b). Case 4: Oblique sea condition (Link: https://youtu.be/e8uIlXfVmlQ)

Figure A.2: Validation results under irregular waves

APPENDIX B

In this section, the S-N curve and stress reduction factor information from Section 2. Analysis of fatigue capacity: DNV-CN 30.7 (DNVGL, 2024) is briefly summarised.

Table B1. S-N parameters for welded joint and base materials

S-N Curve	Material	$N \leq 10^7$		$N \leq 10^7$	
		log $\bar{a}$	m	log $\bar{a}$	m
I	Welded joint	12.164	3.0	15.606	5.0
III	Base Material	15.117	4.0	17.146	5.0
IV	Base Material	12.436	3	12.436	3

Note: I, III = for air and or with cathodic protection, IV = corrosive environment.

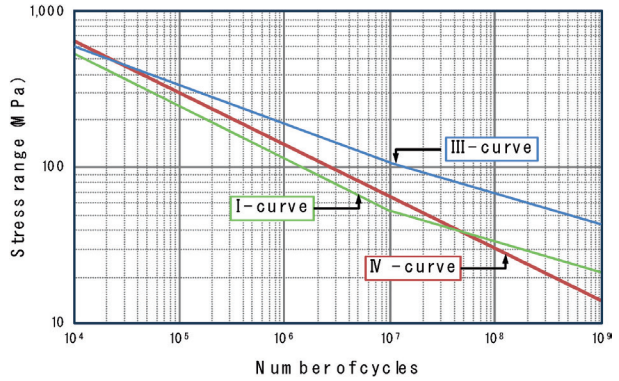

Figure B.1: Three S-N curves based on Table B.1

Fatigue design is carried out based on S-N curves obtained from fatigue tests. The design S-N curves are established from M (Mean) – 2SD (Standard Deviation), reflecting a 97.6% probability of survival. These S-N curves apply to both normal and high-strength steels used in hull structures, and for welded joints, they also include the effect of local weld notches. This means these S-N curves are compatible with calculated stress values that exclude the notch stress caused by the weld. Furthermore, when a butt weld is machined or ground flush without weld overfill, a more favourable S-N curve can be applied. Reference for this is provided in DNV-RP-C203.

The basic design S-N curve is given as

$$\log N = \log \bar{a} - m \log \Delta\sigma$$

with S-N curve parameters given in Table B1.

N Predicted number of cycles to failure for stress range $\Delta\sigma$

$\Delta\sigma$ Stress range

M Negative inverse slope of S-N curve

log $\bar{a}$ Intercept of log N-axis by S-N curve

$$\log \bar{a} = \log a - 2SD$$

where,

a Constant relating to mean S-N curve

SD Standard Deviation of log N, 0.2

Most S-N data come from fatigue testing of small specimens in laboratory settings. For simple test specimens, testing continues until the specimens fail, and no stress redistribution occurs during crack growth. Consequently, the majority of fatigue life is associated with the slow growth of a small crack, which accelerates as the crack enlarges until fracture. Fatigue crack initiation takes longer in a notch within base material than at a weld toe or weld root, meaning that when base material has higher fatigue resistance than welded details, cracks in base material grow faster once initiated. For practical purposes, failures in test data are defined as crack growth through the thickness. When this criterion is applied to actual structures - where stress redistribution is more likely - the failure criterion equates to a crack size slightly less than the plate thickness.

Table B.2: Stress reduction factor (K_p)

K_p	Schematic views	Explanation
0.72		Automatic welding case for both sides
0.80		Automatic fillet welding or butt welding for both sides but containing stop-start positions
	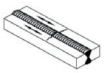	Automatic butt weldings for one side only, with a backing bar, but without start-stop positions.
		
0.90	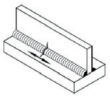	Manual fillet welding or butt welding.
		Manual welding or automatic butt welding for one side only, particularly for box girders
		Repaired automatic or manual fillet or butt weldings

Note: K_p = Stress reduction factor.

The S-N curves in Table B.1 and Figure B.1 are formulated for principal stresses acting normal to the weld and should be used along with the maximum stress range within ±45º of the normal to the weld. If the governing stress direction is parallel to the weld, a stress reduction factor should be applied to the principal stress range before inputting it into the S-N curve. The specific value of will depend on the weld quality, as shown in Table B.2.

The S-N curves in Table B1 are developed for principal stresses acting normal to the weld and should be used with the maximum stress range within ± 45º of the normal to the weld. If the governing stress direction is parallel with the weld direction, a stress reduction factor should be used on the principal stress range before entering stress into the S-N curve. The stress reduction factor will depend on the quality of the weld, Table B2. Once again, it shall be noticed that Appendix B is from DNV-CN 30.7.